

WL-TR-94-5023

ERROR MEASUREMENTS IN AN ACOUSTO-
OPTIC TUNABLE FILTER FIBER BRAGG GRATING
SENSOR SYSTEM

AD-A283 912



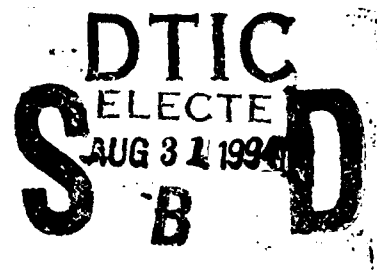
ANTONIO CRESPO

E/O TECHNIQUES & APPLICATIONS BRANCH
SOLID-STATE ELECTRONICS DIRECTORATE
WRIGHT LABORATORY
AIR FORCE MATERIEL COMMAND

MAY 1994

FINAL REPORT FOR 08/01/91-01/01/94

APPROVED FOR PUBLIC RELEASE; DISTRIBUTION IS UNLIMITED.



SOLID STATE ELECTRONICS DIRECTORATE
WRIGHT LABORATORY
AIR FORCE MATERIEL COMMAND
WRIGHT PATTERSON AFB OH 45433-7331

DTIC QUALITY INSPECTED 8

103PX

94-28135



94 8 30 1 63

NOTICE

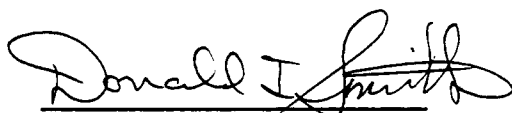
WHEN GOVERNMENT DRAWINGS, SPECIFICATIONS, OR OTHER DATA ARE USED FOR ANY PURPOSE OTHER THAN IN CONNECTION WITH A DEFINITELY GOVERNMENT-RELATED PROCUREMENT, THE UNITED STATES GOVERNMENT INCURS NO RESPONSIBILITY OR ANY OBLIGATION WHATSOEVER. THE FACT THAT THE GOVERNMENT MAY HAVE FORMULATED OR IN ANY WAY SUPPLIED THE SAID DRAWINGS, SPECIFICATIONS, OR OTHER DATA, IS NOT TO BE REGARDED BY IMPLICATION, OR OTHERWISE IN ANY MANNER CONSTRUED, AS LICENSING THE HOLDER, OR ANY OTHER PERSON OR CORPORATION: OR AS CONVEYING ANY RIGHTS OR PERMISSION TO MANUFACTURE, USE, OR SELL ANY PATENTED INVENTION THAT MAY IN ANY WAY BE RELATED THERETO.

This report is releasable to the National Information Service (NTIS). At NTIS, it will be available to the general public, including foreign nations.

THIS TECHNICAL REPORT HAS BEEN REVIEWED AND IS APPROVED FOR PUBLICATION.


ANTONIO CRESPO, EE
E-O Techniques & Appl. Branch
Electro-Optics Division


JOHN O. CRIST, Actg. Chief
E-O Techniques & Appl. Branch
Electro-Optics Division


DONALD J. SMITH, Actg. Chief
Electro-Optics Division
S. S. Electronics Directorate

If your address has changed, if you wish to be removed from our mailing list, or if the addressee is no longer employed by your organization please notify WL/ELOT, WPAFB, OH 45433-7331 to help us maintain a current mailing list.

Copies of this report should not be returned unless return is required by security considerations, contractual obligations, or notice on a specific document.

REPORT DOCUMENTATION PAGE

Form Approved
OMB No. 0704-0188

Public reporting burden for this collection of information is estimated to average 1 hour per response, including the time for reviewing instructions, searching existing data sources, gathering and maintaining the data needed, and completing and reviewing the collection of information. Send comments regarding this burden estimate or any other aspect of this collection of information, including suggestions for reducing this burden, to Washington Headquarters Services, Directorate for Information Operations and Reports, 1215 Jefferson Davis Highway, Suite 1204, Arlington, VA 22202-4302, and to the Office of Management and Budget, Paperwork Reduction Project (0704-0188), Washington, DC 20503.

1. AGENCY USE ONLY (Leave blank)		2. REPORT DATE May 94	3. REPORT TYPE AND DATES COVERED Final, Aug 91 - Jan 94	
4. TITLE AND SUBTITLE ERROR MEASUREMENTS IN AN ACOUSTO-OPTIC TUNABLE FILTER FIBER BRAGG GRATING SENSOR SYSTEM			5. FUNDING NUMBERS PE 62204F PR 2001 TA 05 WU 12	
6. AUTHOR(S) Antonio Crespo				
7. PERFORMING ORGANIZATION NAME(S) AND ADDRESS(ES) E/O Techniques & Applications Branch WL/ELOT Building 22B 2700 D Street suite 2 WPAFB, Oh 45433-7405			8. PERFORMING ORGANIZATION REPORT NUMBER WL-TR-94-5023	
9. SPONSORING/MONITORING AGENCY NAME(S) AND ADDRESS(ES) Solid State Electronics Directorate Wright Laboratory Air Force Materiel Command Wright-Patterson AFB, OH 45433-7331			10. SPONSORING/MONITORING AGENCY REPORT NUMBER WL-TR-94-5023	
11. SUPPLEMENTARY NOTES Thesis submitted to the University of Puerto Rico, Mayaguez Campus				
12a. DISTRIBUTION / AVAILABILITY STATEMENT Approved for public release, distribution unlimited			12b. DISTRIBUTION CODE	
13. ABSTRACT (Maximum 200 words) This final report is a thesis submitted to the University of P.R., Mayaguez Campus. This research analyzed theoretically and experimentally an Acousto-Optic Tunable Filter--Fiber Bragg Grating (AOTF-FBG) system. This analysis was targeted to investigate the measurement error in the AOTF-FBG system.				
14. SUBJECT TERMS Fiber Bragg Grating, Wavelength Division Multiplexing, Acousto-Optic Tunable Filter.			15. NUMBER OF PAGES 102	
			16. PRICE CODE	
17. SECURITY CLASSIFICATION OF REPORT UNCLASSIFIED	18. SECURITY CLASSIFICATION OF THIS PAGE UNCLASSIFIED	19. SECURITY CLASSIFICATION OF ABSTRACT UNCLASSIFIED	20. LIMITATION OF ABSTRACT UNLIMITED	

TABLE OF CONTENTS

TABLE OF CONTENTS	iii
ILLUSTRATIONS	v
TABLES	ix
PREFACE	x
ACKNOWLEDGMENT	xii
1. INTRODUCTION	1
2. LITERATURE REVIEW	3
3. THEORY	8
3.1 Fiber Optic Bragg Gratings	8
3.2 Acousto-Optics	12
3.3 Acousto-Optic Tunable Filter	20
3.4 Acousto-Optic Tunable Filter - Fiber-optic Bragg Grating system ..	30
4. EXPERIMENTATION	38
4.1 Experiment Set-up	38
4.2 Recorded Data and Observations	42
5. RESULTS AND EVALUATION	61
6. CONCLUSION	72
7. FUTURE WORK	75
REFERENCES	76

Accession For	
NTIS GPA&I	<input checked="" type="checkbox"/>
DTIC TAB	<input type="checkbox"/>
Unannounced	<input type="checkbox"/>
Justification	
By	
Distribution/	
Availability Codes	
Dist	Avail and/or Special
A-1	

APPENDIX A: LIA Bandpass Characteristics.	79
APPENDIX B1: Center Frequency Determination Program	81
APPENDIX B2: Data Filtering Program	82
APPENDIX B3: AOTF Simulation Program	86

ILLUSTRATIONS

Figure 2.1. Section of a reflection grating.	4
Figure 2.2. Schematic diagram of an optical spectrum analyzer, from reference [8].	5
Figure 3.1. Setup for making Bragg gratings on optical fibers, from reference [5]	8
Figure 3.2. Acousto-optic up-shift diffraction of light.	13
Figure 3.3. Vector diagram for acousto-optic diffraction.(a) Downshift diffraction, (b) Upshift diffraction.	15
Figure 3.4. Nonideal acousto-optic diffraction.	16
Figure 3.5. K-Vector diagram for an acousto-optic interaction on an isotropic medium (from reference [10]).	17
Figure 3.6. Two possible K-Vector diagrams for acousto-optic interaction in an anisotropic medium. (a) collinear interaction and (b) non-collinear interaction (from reference [10]).	18
Figure 3.7. Acousto-optic modulation.	29
Figure 3.8. Modulation frequency response for analog acousto-optic modulation.	30
Figure 3.9. AOTF-FBG system configuration for a two-channel sensor fiber.	31
Figure 3.10. Single channel bandpass levels for an ideal AOTF centered at 833 nm using a TeO ₂ crystal.	33
Figure 3.11. Multiple channels bandpass levels for an ideal AOTF, at 833 and 838 nm using a TeO ₂ crystal.	33
Figure 3.12. Frequency characteristics of Equation (3.43) with $\omega_m = 2\pi * 300$ Hz, amplitude is in dB.	34

Figure 3.13. Frequency characteristics of Equation (3.42) with $f_1 = 300$ Hz and $f_2 = 200$	35
Figure 3.14. Ideal reflection of a FBG, Equation (3.2), with a FWHM of .1 nm.	36
Figure 3.15. Convolution between the FBG function (Equation (3.2)) and the ideal AOTF function.	37
Figure 4.1. Schematic set-up of experiment.	38
Figure 4.2. AOTF's filter response of a square wave amplitude modulation. The scales are 200 μ V/div and 1 ms/div.	42
Figure 4.3. Spectra Diode Labs Laser model SDL-2410.	44
Figure 4.4. Optical spectrum of Sharp's laser diode model LTO15MD. . . .	45
Figure 4.5. Bandpass of the AOTF.	46
Figure 4.6. Bandpass of the AOTF with two RF frequencies.	47
Figure 4.7. SRD-8300 spectrum when passing through the FBG.	48
Figure 4.8. RF spectrum of two oscillators. A fix oscillator was set to 149.157 MHz and 300 Hz AM and a sweep oscillator was set to a fixed frequency of 149.410 MHz and 100 Hz AM.	49
Figure 4.9. RF spectrum of two oscillators. One fix oscillator was set to 149.157 MHz and 300 Hz AM and a second fix oscillator was set to a frequency of 149.4025 MHz and 100 Hz AM.	49
Figure 4.10. RF spectrum of two oscillators. One fix oscillator was set to 149.157 MHz and a second fix oscillator was set to a frequency of 149.4025 MHz. No modulation was used.	50
Figure 4.11. Data taken with sinusoidal amplitude modulation. Intensity scale is 1 mV/4095.	51
Figure 4.12. Data taken with a square wave amplitude modulation. Intensity scale is 1 mV/4095.	51

Figure 4.13. Data taken with a square wave amplitude modulation on only one channel. Intensity scale is 1 mV/4095.	52
Figure 4.14. Amplification of the frequency plot in Figure 4.11.	52
Figure 4.15. Sweep plot with sinusoidal amplitude modulation. Intensity scale is 1 mV/4095 for the 300 Hz and 2 mV/4095 for the 260 Hz signal.	54
Figure 4.16.. Data showing a wavelength transition in the Sharp's diode. Sinusoidal amplitude modulation and the intensity scale is 2 mV/4095 for the 257 Hz and 1 mV/4095 for the 300 Hz signal.	55
Figure 4.17. Wavelength scan on the Sharp's laser diode with a sinusoidal AM. LIA was set at $Q = 100$, the intensity scale is 1 mV/4095 for the 303 Hz and 2 mV/4095 for the 262 Hz signal.	56
Figure 4.18. Wavelength scan on the Sharp's laser diode with a sinusoidal AM. LIA was set at $Q = 100$, the intensity scale is 1 mV/4095 for the 303 Hz and 2 mV/4095 for the 284 Hz signal.	56
Figure 4.19. Wavelength scan on the Sharp's laser diode with a square wave AM. LIA was set at $Q = 100$, the intensity scale is 1 mV/4095 for both signals.	57
Figure 4.20. Wavelength scan on both laser diodes with a sinusoidal AM. LIA was set at $Q = 100$, the intensity scale is 1 mV/4095 for both signals.	58
Figure 4.21. Detector output with single frequency present. The scales are 100 μ V/div and 5 mS/div.	59
Figure 4.22. Detector output with multiple frequencies present. The scales are 100 μ V/div and 5 mS/div.	59
Figure 5.1. Theoretical response of the AOTF to a square wave modulation (Equation 5.2).	61
Figure 5.2. Modulating frequency response of the AOTF's resonant cavity.	62
Figure 5.3. Zoom of the peak portion of the data on Figure 4.17.	64

Figure 5.4. The data on Figure 5.3 after filtering.	64
Figure 5.5. Mathematical model of the AOTF output at 105 Hz AM frequency.	68
Figure 5.6. Mathematical model of the AOTF output with two signal input, 105 and 298 Hz AM frequency.	69
Figure 5.7. Calculated bandpass of the LIA, amplitude is in dB.	69
Figure 5.8. Minimum distance between optical signals.	70
Figure 5.9. Zoom and filtering of the data on Figure 4.15.	71
Figure 5.10. Zoom and filtering of the data on Figure 4.18.	71
Figure A.1. Frequency bandpass characteristics of the LIA Model 124A, as stated by the manufacturer.	79
Figure A.2. Phase bandpass characteristics of the LIA Model 124A, as stated by the manufacturer.	80

TABLES

Table 4.1. Specifications of the AOTF	39
Table 5.1. FWHM calculation of the AOTF	63
Table 5.2. Measurement Errors	65

PREFACE

Fiber-Optic embedded sensors can serve as an effective nervous system for smart skins. The sensor type used in this investigation is the United Technology Photonic's Fiber Bragg Grating (FBG) sensor. A great advantage of these sensors is that they can be wavelength multiplexed along a single fiber. The problem is to determine the reflected wavelength from the sensors in a fast way with a compact and rugged system, but with high accuracy. An Acousto-Optic Tunable Filter (AOTF) system was investigated to determine its suitability to interrogate the FBG sensors in a fast and accurate manner. One of the advantages of the AOTF is its ability to simultaneously filter multiple channels. Having multiple channels in an AOTF requires the presence of multiple RF frequencies to establish the complex grating. Since the crystal used in the AOTF (TeO_2) is a *non-linear acoustic material*, the multiple frequencies will create undesirable harmonics which will degrade the performance of the device. To separate the channels, the RF signals are AM modulated. This creates additional harmonics. The objective of this thesis was to determine if the harmonics present in a multiple channel AOTF presents a problem in determining the reflected Bragg wavelength. Also, the speed of the system was determined. A comparison was made using a commercially available spectrometer.

For the two RF carrier signals in the AOTF, the errors due to second harmonics were not detectable with the current instruments. This indicates that the value of the acoustic non-linear parameter is small. The Lock-In Amplifier (LIA) bandpass characteristics limited the minimum separation between the modulating frequencies at 0.13 times the highest modulating frequency. The AM signals had to be chosen so that their strongest harmonics didn't overlap with the signals. The amplitude of the sidelobes determines how close two channels can be from each other. The RF sweeper imposed another $\approx \pm 0.02\text{nm}$ error (3-4

KHz) in the signal. A limiting factor in the AOTF's scanning speed turned out to be its resonance behavior. This limited the amplitude modulation to 300 Hz and a maximum switching speed of 3.33 ms. Improvements need to be made to the design of the AOTF to increase its cut off frequency and the efficiency per channel. The current AOTF could, at most, have two channels with a diffraction efficiency of $\approx 28\%$.

ACKNOWLEDGMENT

I wish to avow the contributions of a number of individuals whose help was invaluable for the completion of this undertaking.

The chief scientist of our branch, Mr. Joseph E. Brandelik, was the visionary that conceived this experiment and furnished a number of suggestions in the direction of this work. The custom made components used in this experiment were fabricated and designed by Sam Leforge. His machining skills and insight were extremely helpful in devising solution to problems. Mr. Dale M. Stevens guided me in the utilization and handling of the fiber-optic components. I would also like to thank Dr. Ken Schepler and Mr. Robert Wade for the utilization of the optical spectrum analyzer. Also the support of my branch (Wright Lab /Electro-Optics Techniques and Applications) without which this experiment may not have been performed. Also a special thanks to my wife Nelly and my new born daughter, Cristina, for their support throughout this thesis.

1. INTRODUCTION

The purpose of the research presented in this thesis was to determine the limitations of an AM modulated Acousto-Optical Tunable Filter (AOTF) when used as a spectrum analyzer with multiple channels. Also, to make a comparison between the AOTF and a commercial spectrum analyzer in speed and accurateness. The spectrum analysis is to be used in determining the reflected wavelength from the Fiber Bragg Grating sensors. Up to this point the behavior of a multiple channel AM modulated AOTF has not been investigated. The AM modulation in the channels will have the advantage of making them electronically separable.

Optical fibers are being widely used for communications because of their long distance transmission capability and immunity to electromagnetic interference. During the past 15 years optical-fiber sensors have been under development. Optical fiber sensors are electrically passive and light weight. In a fiber sensor, a beam of light is sent through the fiber(s) where it is modified, due to an external force, and this modification is detected. The applications of these sensors^[1] range from stress and temperature monitoring to process control of flow, pressure, and liquid level in industrial systems. One application is in "smart structures" for distributed strain and temperature sensing of aircraft. In the smart structures concept, the fibers are embedded in the structure to be monitored. Up to recently, the strain measurements were done using phase interference

techniques^[1]. There is no residual memory in such techniques, and they detect the strain along the total length of the fiber. These techniques detect the change in strain if the system is running. Any strain developed while the system is off will not be detected. Therefore, the cumulative stress on the structures lifetime cannot be measured (unless the system is always on). Also, two fibers of equal length are needed, one being the sensing fiber and the other the reference fiber.

Fiber Bragg Grating sensors promise to solve these problems. With this type of sensor, strain and temperature can be monitored in a localized region of the optical fiber. In addition, the cumulative strain and temperature change that occurs while the system is off can be determined. The monitoring system analyzed in this research is based on an Acousto-Optic Tunable Filter (AOTF). The AOTF is used as a spectrum analyzer. Using the AOTF has the benefits that it is compact and rugged. In addition, it can operate multiple channels simultaneously and independently.

2. LITERATURE REVIEW

In 1978, Hill and coworkers discovered that narrow bandwidth Bragg gratings could be created within the Ge-doped core of certain optical fibers using green light from an argon ion laser^[2]. This photosensitivity has been observed to be even stronger when ultraviolet light is used to irradiate the optical fiber^[3,4,5]. The formation of these Bragg gratings results from a periodic perturbation of between 10^{-5} and 10^{-4} in the refraction index along the fiber core. These intra core gratings are written by sideways exposure of the core to ultraviolet light in the form of an interference pattern^[2]. These gratings form the basis of an important new class of optical sensors. The lack of a compact and rugged system that can rapidly determine this bragg wavelength has severely limited the use of the intracore Bragg gratings as practical sensors.

The principle of acousto-optic diffraction is similar to that of a transmission diffraction grating^[6]. As such, it is possible to use an acousto-optic Bragg cell as the dispersive element in an optical spectrometer. In a diffraction grating a repetitive array of elements, see Figure 2.1, has the effects of producing periodic alteration in the phase, amplitude, or both on an emergent wave. The diffraction grating acts similar to a prism diffracting light of different wavelengths at different angles. The distance between the elements in a diffraction grating is known as the grating constant, parameter a in Figure 2.1^[7]. In the acousto-optic grating, the grating constant is equal to the acoustic wavelength. One obvious advantage of

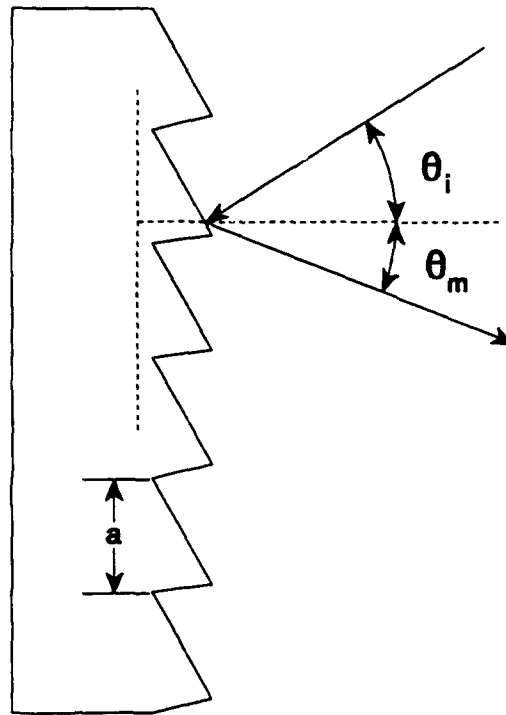


Figure 2.1. Section of a reflection grating.

an acousto-optic grating spectrometer is that the grating constant can be changed electronically, thus providing a capability of rapidly scanning the spectral region at an observation point. As for a single detector diffraction grating spectrometer the diffraction grating has to be physically rotated to scan a spectral region through an observation point. To minimize the mechanical movement a linear array of detector elements could be used, therefore having a fast scan of a particular region, but to change regions the grating needs to be rotated. One drawback of the diffraction grating spectrum analyzer is the size and precise alignment it needs. In a diffraction grating the angular positions of the non-zero orders, θ_m values, are determined by a , λ , and θ_i , and is given by the following equation:^[7]

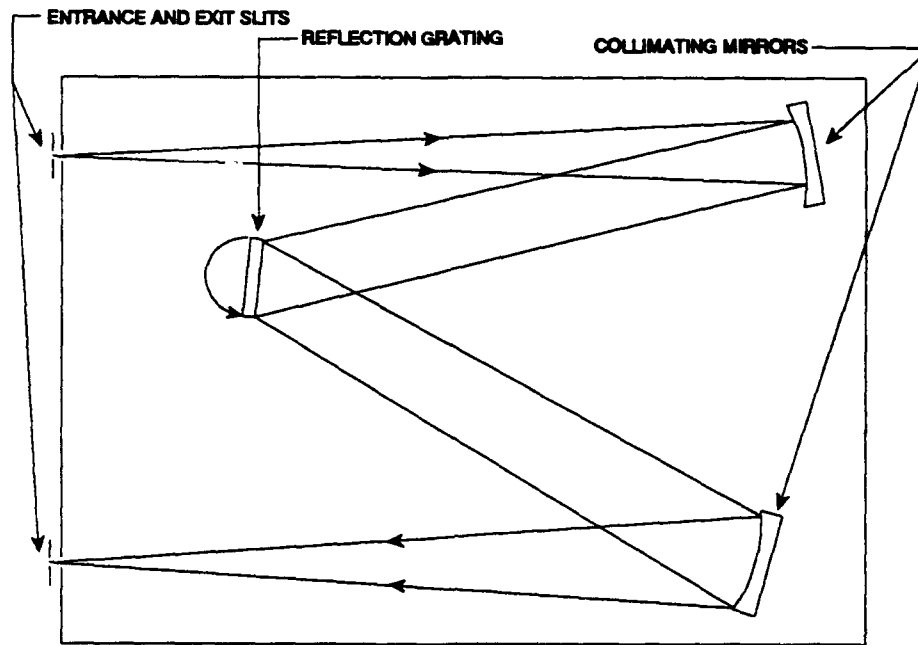


Figure 2.2. Schematic diagram of an optical spectrum analyzer, from reference [8].

$$a(\sin \theta_m - \sin \theta_i) = m\lambda \quad (2.1)$$

where θ_m and θ_i are measured from the normal of the grating plane and not with the individual groove surfaces.

In a typical single detector diffraction grating spectrum analyzer^[8], light is collimated onto a holographic or ruled grating by a curved mirror, see Figure 2.2. A reflection grating with groove spacing, a , will disperse the incident light into a series of angles, θ_m , according to Equation 2.1.

The angle of incidence, θ_i , is determined by the geometrical arrangement of elements in the spectrometer and does not affect the resolution or accuracy. For maximum precision, grating rotation is achieved by a computer-controlled stepper

motor. In this manner θ_m and θ_i can be determined to high accuracy, thereby allowing the wavelength λ to be computed.

The Acousto-Optic tunable filter (AOTF) is based on acoustic diffractions of light in an anisotropic medium^[9,10]. The device consists of a piezoelectric transducer bonded to a birefringent crystal. When the transducer is excited by an applied RF signal, acoustic waves are generated in the medium. The propagating acoustic wave produces a periodic modulation of the index of refraction. This provides a moving phase grating, which establishes an anisotropic Bragg diffraction mechanism^[9], that, under proper conditions^[10], will diffract portions of an incident light beam. This anisotropic diffraction necessarily involves rotation of the polarization plane of the diffracted wave. For a fixed acoustic frequency, only a limited band of optical frequencies can satisfy the phase-matching condition and be cumulative diffracted. As the RF frequency is changed, the center of optical passband is changed accordingly so that the phase-matching condition is maintained. An advantage of the AOTF is the fact that multiple RF frequencies can be used to establish a complex grating pattern within the crystal^[11]. This will diffract multiple bands of light corresponding to the multiple RF frequencies. Another advantage of the AOTF is its compactness.

Being an anisotropic acoustic (as well as optical) material there will be harmonics created which might diffract additional bands and create noise. Since the filtering of light from an RF input signal is not a linear process, there will be additional harmonics created when the signal is amplitude modulated. These AM

modulation related harmonics will also create noise which will affect the determination of the peak wavelength.

3. THEORY

3.1 Fiber Optic Bragg Gratings

Recently there has been a new development in fiber optic sensors. United Technologies Photonics has developed a way to bleach Bragg grating sensors, called Fiber-optic Bragg Gratings (FBG), into optical fibers^[3,4]. The gratings are formed by exposing the side of a germania doped fiber core to a high intensity (4 - 20 mW average power) interference pattern of UV, close to 244 nm, light, Figure 3.1^[5]. This interference pattern impresses a permanent index modulation in the

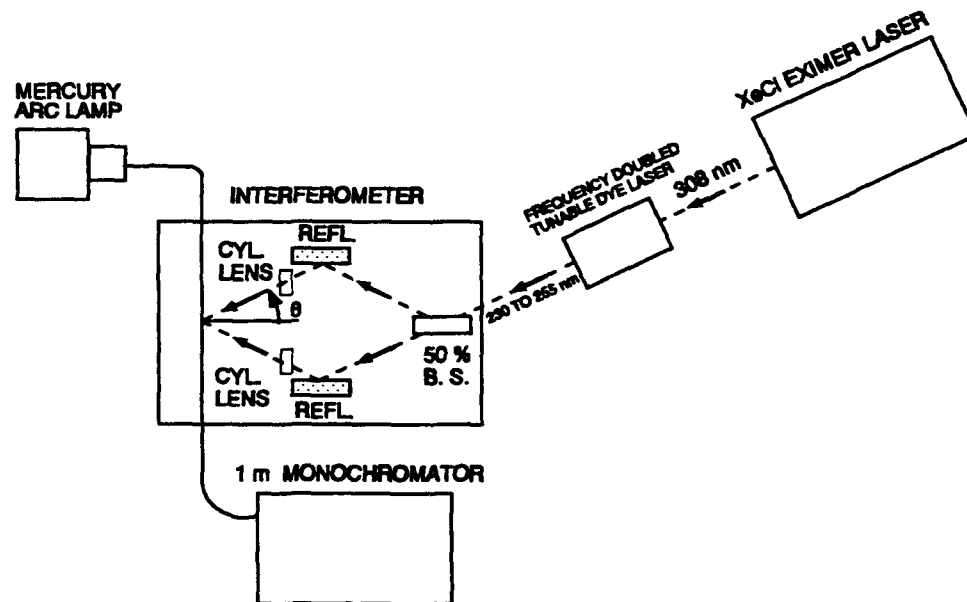


Figure 3.1. Setup for making Bragg gratings on optical fibers, from reference [5]

fiber core by bleaching the oxygen vacancy defect absorption band in germano-silicate glass. This index modulation, Bragg grating, acts as an optical band rejection filter for those wavelengths that meet the Bragg condition:

$$\lambda_{ob} = 2n_e d \quad (3.1)$$

where λ_{ob} is the wavelength (in vacuum) of the center peak notch, d is the grating period and n_e is the effective index of refraction of the fiber mode. Mode coupling theory can be of use in a periodic wave guide to model the grating filter^[12,13]. The reflectance as a function of wavelength and filter length is given by^[12,13]

$$R = \left| \frac{-\Omega \sinh(SL)}{(\frac{\alpha}{2} + j\Delta\beta) \sinh(SL) + S \cosh(SL)} \right|^2 \quad (3.2)$$

where

$$\begin{aligned} S &= \sqrt{\Omega^2 - (\Delta\beta - j\frac{\alpha}{2})^2} \\ \Omega &= \frac{\pi \Delta n \eta(V)}{\lambda} \\ \eta(V) &= 1 - \frac{1}{V^2}, \quad V \geq 2.4 \\ \Delta\beta &= \beta - \frac{\pi}{d} \end{aligned} \quad (3.3)$$

L is the filter length, β is the longitudinal propagation factor of the optical beam, α is the attenuation coefficient of the waveguide, V is the normalized frequency of the waveguide, and Δn is the magnitude of the index perturbation.

Top view of the set-up^[5] used to fabricate the Bragg gratings through the side of the optical fibers, is shown in Figure 3.1. Under this set-up the Bragg wavelength is given by

$$\lambda_{ob} = \frac{\lambda_i n_e}{\sin \theta} \quad (3.4)$$

where n_e is the effective index of refraction of the fiber mode, λ_i the UV wavelength used to generate the grating and θ the half angle of the intersecting UV beams. As can be seen, the reflected Bragg wavelength can be determined by adjusting θ or (up to a certain degree) λ_i .

If the FBG is subjected to a temperature change this will produce a change in the Bragg's wavelength due to thermal expansion and to a change in the index of refraction. The wavelength change due to temperature change is given by the following formula:^[5]

$$\frac{\Delta \lambda_b}{\lambda_b} = (\alpha + \xi) \Delta T \quad (3.5)$$

where α is the thermal expansion coefficient for the fiber (equals $0.55 \times 10^{-6}/^{\circ}\text{C}$ for silica) and ξ represents the thermo-optic coefficient (it is approximately equal to $8.3 \times 10^{-6}/^{\circ}\text{C}$ for the germania doped silica core), and ΔT is in $^{\circ}\text{C}$. The Bragg's wavelength change due to index change is far greater than the change due to

thermal expansion. This is true when the fiber is subjected to temperature changes only. The calculated results using this Equation are smaller than the actual results obtained from a fiber^[5]. It is speculated that the difference is due to inaccurate thermo-optic coefficient and/or possible strain relief of the fiber core when the fiber is heated.

When the FBG is subjected to strain, the center frequency of the reflected wavelength changes due to a change in the grating spacing and in the index of refraction. The change in the index of refraction is due to the photo-elastic effect on the fiber. The center wavelength change due to longitudinal strain ϵ is given by:^[5]

$$\Delta\lambda_b / \lambda_b = (1 - p_e)\epsilon \quad (3.6)$$

where p_e is:

$$p_e = (n^2/2)[p_{12} - \nu(p_{11} + p_{12})] \quad (3.7)$$

and is the effective photo-elastic constant (and is ≈ 0.22 for germanosilicate glass), p_{12} and p_{11} are components of the contracted orthotropic strain-optic tensor (the subscripts refer to the coordinate axis of the optical fiber, 1 is the direction along the fiber), n is the index of the core, and ν the Poisson's ratio. The calculated change in the Bragg wavelength is greater than the actual change^[5]. It is speculated that the difference is due to uncertainties in the photo-elastic constant caused by a high concentration of germanium doping in the core of the fiber.

3.2 Acousto-Optics

Acousto-Optics deals with the interaction of light with sound waves in a medium. A sound wave consists of sinusoidal perturbations of strain or density of the medium. These perturbations create an index modulation in the medium, due to the photo-elastic effect, which generates a moving phase grating that may diffract light in one or more directions. The diffraction will depend whether or not the light is incident at a critical angle α_c . The direction of diffraction will be determined by the grating constant (which is equal to the acoustic wavelength) of this acoustically generated grating. This electronically generated grating can be used as the dispersive element on a spectrometer.

Particle physics, conservation of momentum, and conservation of energy will be used to understand how the acoustic waves diffract light⁽¹⁴⁾. Let us consider a light beam with a wave vector \mathbf{k}_i and frequency ω_i incident on a crystal at an angle α_i as shown on Figure 3.2, the refraction effects are not shown on the figure. Also let's have a sinusoidal acoustic wave of wave vector \mathbf{K}_a and acoustic frequency ω_a traveling along the width of the crystal, the acoustic wave fronts are moving away from the light beam and it is assumed that these are planar waves. Inside the crystal an incident photon with momentum $\hbar\mathbf{k}_i$ (where $\hbar = h/2\pi$, h is Planck's constant) collides with a phonon with momentum $\hbar\mathbf{K}_a$. Both of these are annihilated in the process, creating a diffracted photon with momentum $\hbar\mathbf{k}_d$, i.e.,

$$\hbar\mathbf{k}_i + \hbar\mathbf{K}_a = \hbar\mathbf{k}_d \quad (3.8)$$

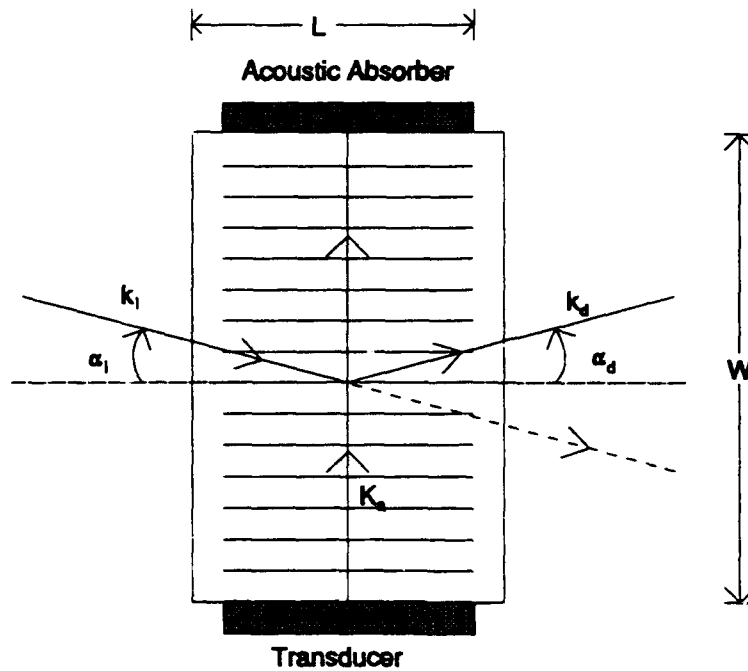


Figure 3.2. Acousto-optic up-shift diffraction of light.

In energy terms this particular situation is described by:

$$\hbar\omega_i + \hbar\omega_a = \hbar\omega_d \quad (3.9)$$

From Equations (3.8) and (3.9), it can be seen that the new photon created has shifted up in frequency by ω_a as well as increased the wave vector by K_a . This is called the upshift diffraction process and the diffracted beam is called the +1 order.

Now if the direction of propagation of the sound waves is reversed, the path of the light beams will remain the same, a little different process takes place. The

collision of the two particles (the phonon and the photon) will produce two phonons (each one with the same energy and direction as the initial phonon) and a photon. This photon will be diffracted towards a different direction than the initial photon. The diffracted photon will have less momentum than the incident photon. As it can be seen in the following Equation:

$$\hbar k_i + \hbar K_a = \hbar K_a + \hbar K_a + \hbar k_d \quad (3.10)$$

Rewriting the formula for the wave vector:

$$k_d = k_i - K_a \quad (3.11)$$

going through the same steps but using the conservation of energy equation the following frequency relationship can be obtain:

$$\omega_d = \omega_i - \omega_a \quad (3.12)$$

For this situation the frequency of the diffracted beam of light is down shifted by ω_a . This is called downshift diffraction process accordingly and the diffracted beam the -1 order. Figure 3.3 illustrates the upshift and the downshift diffraction in vector diagrams^[15].

Since $\omega_i \gg \omega_a$ Equations (3.8), (3.9), (3.11) and (3.12) are reduced to^[14]:

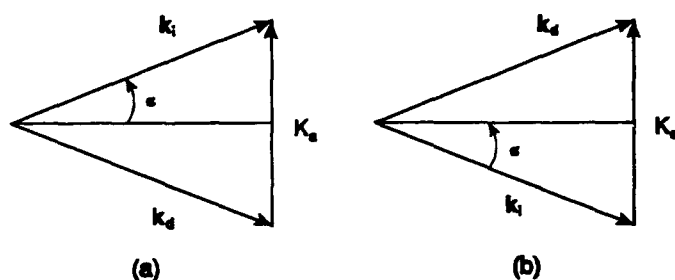


Figure 3.3. Vector diagram for acousto-optic diffraction. (a) Downshift diffraction, (b) Upshift diffraction.

$$\begin{aligned}\omega_i &\approx \omega_d \\ k_i &\approx k_d\end{aligned}\tag{3.13}$$

From Figure 3.3 and Equation (3.13) one can easily obtain the relationship between the angle and the wavelength to be:

$$\frac{\lambda}{\Lambda_a} = 2 \sin \alpha\tag{3.14}$$

Where λ is the wavelength in the acoustic medium, and Λ_a is the acoustic wavelength in the crystal (which is equal to the grating constant).

Note that all these calculations were done under the assumption of having purely planar acoustic waves. In reality for this to occur $L \rightarrow \infty$ (Figure 3.2), or a large interaction length needs to be present. Decreasing the interaction length will make the acoustic waves depart from an ideal case, i.e., non-planar waves Figure 3.4. These non-ideal waves can be model as adding additional plane waves moving in different directions. The effect of these additional waves is that now

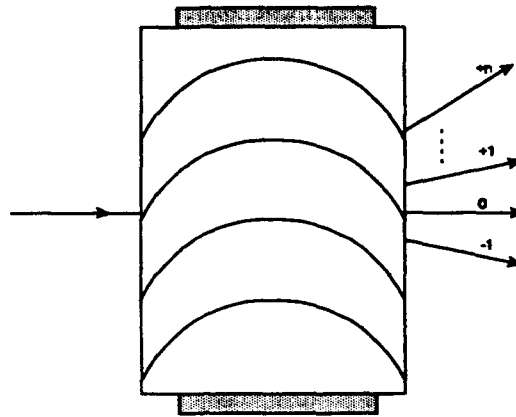


Figure 3.4. Non-ideal acousto-optic diffraction.

both the +1 & -1 diffraction orders are now present. If the interaction length is reduce further additional orders will become present. These diffracted beams of light will have a frequency and a wave vector corresponding to:

$$\begin{aligned}\omega_{dm} &= \omega_i + m\omega_a \\ \mathbf{K}_{dm} &= \mathbf{k}_i + m\mathbf{K}_a\end{aligned}\tag{3.15}$$

where $m = \pm 1, \pm 2, \pm 3, \dots, \pm n$ is the diffraction order. If there is multiple diffraction it is said that the device is working in the Raman-Nath regime while if the opposite condition is true it is said to be operating in the Bragg regime. The parameter Q is used to determine the regime that the device will be operating at. This parameter is defined by:

$$Q = \frac{K^2 L}{k} = 2\pi \frac{\lambda L}{\Lambda^2}\tag{3.16}$$

If $Q \gg 1$ the device is said to be working in the Bragg region, otherwise it will be working in the Raman-Nath regime.

The angular aperture of an isotropic Acousto-Optic diffraction spectrometer is proportional to the optical bandwidth and is exceedingly small^[10]. This can be viewed with the help of the K-vector diagram shown in Figure 3.5. It can be observed in this diagram that if the incident angle of the optical beam is changed there will be a resulting momentum mismatch Δk . This momentum mismatch will decrease the diffraction efficiency on the isotropic medium thus the angular aperture on an isotropic medium is quite small.

It is indicated in reference [10] that Dixon first investigated acousto-optic diffraction in an anisotropic medium in which the index of refraction is dependent

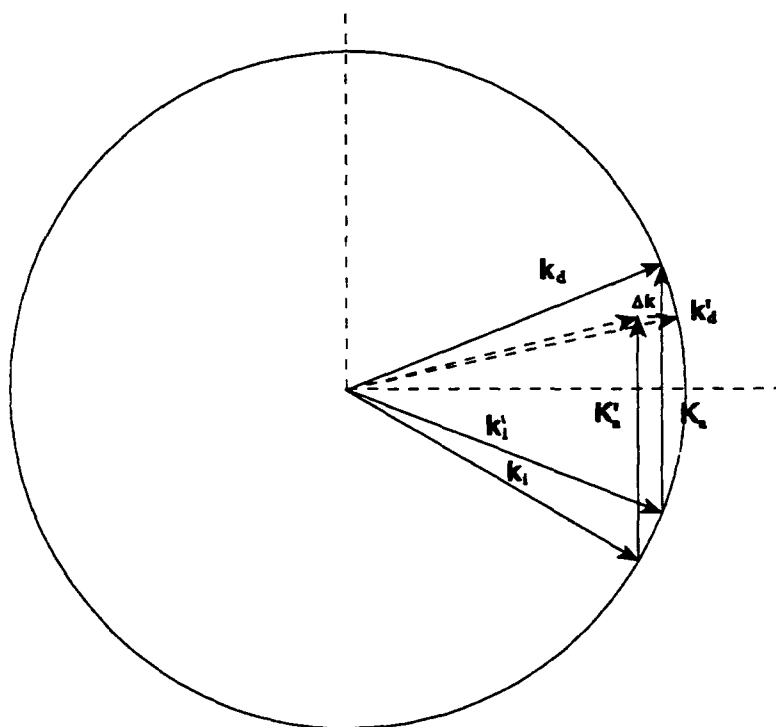


Figure 3.5. K-Vector diagram for an acousto-optic interaction on an isotropic medium (from reference [10]).

on the direction of propagation and polarization of the optical beam. Utilizing anisotropic crystals it has been possible to increase considerably the angular aperture of the acoustic devices^[10]. Two special schemes are shown in Figure 3.6 in which the angular aperture for acousto-optic filtering is increased in an anisotropic. In Figure 3.6(a) a collinear interaction in anisotropic medium is illustrated in K-vector space. In this type of interaction both the optical and acoustic waves are collinear and propagating perpendicular to the optic axis. In the collinear interaction the incident light is linearly polarized. Once the beam

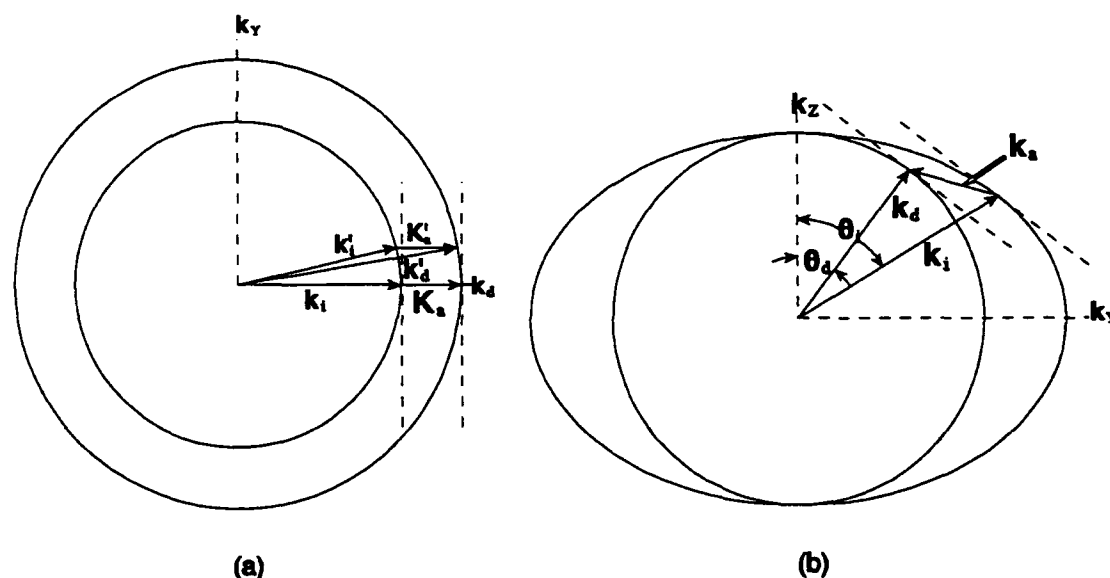


Figure 3.6. Two possible K-Vector diagrams for acousto-optic interaction in an anisotropic medium. (a) collinear interaction and (b) non-collinear interaction (from reference [10]).

enters the crystal it interacts with the acoustic waves and changes the polarization of the waves that matches the following formula

$$\lambda = \frac{V_a \Delta n}{f_a} \quad (3.17)$$

The separation of the incident light and the diffracted light is done using a polarizer. In Figure 3.6(b) a non-collinear interaction is illustrated. In the non-collinear interaction the diffracted beam's wavevector has a different angle than that of the incident beam. But, the tangents to the incident and diffracted wavevector loci are parallel by properly choosing the acoustic wavevector. This is a generalization of the collinear scheme. In both of these schemes you can observe that a first degree change in the incident angles will produce a negligible momentum mismatch. This holds as long as the tangents to the loci of the light wave vectors are parallel.

It is indicated in reference [6] that Harris and Wallace further investigated anisotropic collinear beams interaction. They pointed out that the diffraction light into its orthogonal polarization state occurs only to a small band of optical frequencies along the center wavelength given by Equation (3.17). Thus by changing the acoustic frequency the band-pass region is tuned over a large range of frequencies. They demonstrated this in a series of experiments that they conducted. This forms the principle of collinear Acousto-Optic Tunable Filters (AOTF). From here on the term AOTF will be applied to optical spectrum band-pass filters based on anisotropic acousto-optic interactions. The realization of

non-collinear AOTF with large angular aperture has been realized by Chang^[16]. This type of AOTF is based on the compensation on momentum mismatch due to the change of angle of the incident light by the angular change of birefringence. Figure 3.6(b) illustrates the operation of the non-collinear AOTF in vector space.

3.3 Acousto-Optic Tunable Filter

3.3.1 AOTF Characteristics for Single Frequency.

In the previous section, the theory behind acoustic interaction up to the development of the AOTF was discussed. In this section the theory of the AOTF will be discussed more in depth. To simplify calculations, Chang's^[17] approach of fourier transforms to specify the AOTF's working characteristics will be used. In this approach the acoustically driven spatial modulation along the optical wave propagation direction is decomposed into a spectrum of spatial frequencies. The optical frequencies being filtered by the AOTF can then be determined using the phase matching condition (Equation (3.11)). Where for the birefringent medium the magnitudes of the vectors are given by:

$$k_i = \frac{2\pi n_i}{\lambda_o}, \quad k_d = \frac{2\pi n_d}{\lambda_o}, \quad K_a = \frac{2\pi f_a}{V_a} \quad (3.18)$$

where n_i and n_d are the refractive indices of the incident and diffracted light. λ_o is the optical wavelength in the vacuum, f_a and V_a are the acoustic frequency and velocity respectively. Utilizing Equation (3.18) and the assumption that the

acoustic wavelength is much larger than the optical wavelength, Equation (3.11) can be rewritten as ^[17]:

$$\frac{n_i - n_d}{\lambda_o} = s \quad (3.19)$$

where s is the frequency of the longitudinal spatial modulation along the light propagation direction, which will be denoted as the Z-axis to simplify calculations. The acoustic spatial modulation in the crystal can be expressed as:

$$m(z) = w(z) e^{j[2\pi \frac{f_a}{V_a} z \cos \psi]} \quad (3.20)$$

where $w(z)$ is the slowly varying amplitude function of the spatial modulation. ψ is the angle between the acoustic wave and the Z-axis. Parseval's Theorem can be used to associate the power in the signal with the power contained in each discrete frequency component. The energy spectrum density of Equation (3.20) is thus given by:

$$\begin{aligned} H(s) &= \left| \int_{-\infty}^{\infty} m(z) e^{-j2\pi s z} dz \right|^2 \\ &= \left| W\left(s - \frac{f_a}{V_a} \cos \psi\right) \right|^2 \end{aligned} \quad (3.21)$$

where $W(s)$ is the Fourier transform of $w(z)$ (s is used to denote spacial frequency and not to be confused with temporal frequency). Equation (3.21) yields the bandpass response of the AOTF. By making the following substitution.

$$H(\lambda_o) = |W(\Delta s)|^2 \quad (3.22)$$

therefore

$$\Delta s = \frac{(n_i - n_d)}{\lambda_o} - \frac{f_a}{V_a} \cos \psi \quad (3.23)$$

where Δs is the deviation of spatial frequency from the exact phase matching condition. The coordinate system will now be changed, the optical axis of the crystal will now be the Z-axis. If θ is the polar angle (the angle between the optical, Z, axis and the vector) and ϕ the azimuth angle, Equation (3.23) can be rewritten as:

$$\Delta s = \frac{(n_i - n_d)}{\lambda_o} - \frac{f_a}{V_a} (\cos \theta_i \cos \theta_a + \sin \theta_i \sin \theta_a \cos(\phi_i - \phi_a)) \quad (3.24)$$

Let's consider the specific case of an extraordinary (e) polarized light incident on a uniaxial crystal. For most of the crystals the fractional birefringence is small so the following can be written ^[17]

$$n_i \approx n_o + \Delta n \sin^2 \theta_i \quad (3.25)$$

where $\Delta n = |n_e - n_o|$ is the birefringence. Equation (3.24) can be written as

$$\Delta s = \frac{(\Delta n \sin^2 \theta_i)}{\lambda_o} - \frac{f_a}{V_a} (\cos \theta_i \cos \theta_a + \sin \theta_i \sin \theta_a \cos(\phi_i - \phi_a)) \quad (3.26)$$

For proper filter operation over a large angular aperture, it is required that the 1st-order derivative of Δs with respect to θ_i be zero. If $\phi_i = \phi_a$ the following is obtained^[18]

$$\lambda_o = \frac{V_a \Delta n \sin 2\theta_i}{f_a \sin(\theta_a - \theta_i)} \quad (3.27)$$

at the center of the filter bandpass, $\Delta s = 0$; therefore

$$\lambda_o = \frac{V_a \Delta n \sin^2 \theta_i}{f_a \cos(\theta_a - \theta_i)} \quad (3.28)$$

From Equations (3.27) and (3.28) it can be shown that

$$\tan \theta_i \tan(\theta_a - \theta_i) = 2 \quad (3.29)$$

this defines the relation between the propagation directions of optical and acoustic waves to ensure that the momentum mismatch of the non-collinear is, to first order, independent of the angular divergence of the incident light^[18]. Utilizing Equation (3.29) θ_a can be eliminated from Equations (3.27) and (3.28) to obtain the relation between the center wavelength of the filter bandpass and the driving acoustic frequency for a given light incidence angle^[18]:

$$\lambda_o = \frac{V_a \Delta n}{f_a} (\sin^4 \theta_i + \sin^2 2\theta_i)^{1/2} \quad (3.30)$$

When $\theta_i = 90^\circ$ Equation (3.30) reduces to the simple expression for collinear interaction AOTF (Equation (3.17)).

When Equation (3.29) is satisfied the Taylor series expansion of the incident angular and wavelength deviation ($\Delta \theta_i$, $\Delta \phi_i$, and $\Delta \lambda_i$) of Equation (3.26) reduces to^[17]

$$\Delta s(\Delta\lambda_i, \Delta\theta_i, \Delta\phi_i) = -\frac{b \sin^2 \theta_i}{2\pi} \left(\frac{\Delta\lambda_i}{\lambda_o^2} \right) + \frac{\Delta n}{2\lambda_o} [F_\theta (\Delta\theta_i)^2 + F_\phi ((\sin\theta_i) \Delta\phi_i)^2] \quad (3.31)$$

where b is the dispersive constant given by

$$b = 2\pi \left(\Delta n - \lambda_o \frac{\partial \Delta n}{\partial \lambda_o} \right) \quad (3.32)$$

and

$$F_\theta = 2 \cos^2 \theta_i - \sin^2 \theta_i, \quad F_\phi = 2 \cos^2 \theta_i + \sin^2 \theta_i \quad (3.33)$$

The dispersive constant b may be obtained by differentiating the Sellmeier dispersion formula. Equation (3.31) shows the filter bandpass behavior as a deviation from the calculated parameters is made.

For the special case^[17] of an acoustic column of uniform amplitude and interaction length L , Equation (3.22) gives us the normalized diffracted light intensity:

$$H(\lambda_o) = I_o \operatorname{sinc}^2 \Delta s L \quad (3.34)$$

where I_o is the peak transmission and $\operatorname{sinc}(x) = \sin(\pi x)/(\pi x)$. The half peak transmission, for this situation, occurs when $\Delta s \approx 0.45$ ^[17]. The Full Width at Half Maximum (FWHM) of the AOTF bandpass is then given by

$$\text{FWHM} = \frac{1.8\pi\lambda_o}{bL\sin^2\theta_i} \quad (3.35)$$

Notice that Equation (3.35) shows that an increase in the interaction length, L , will decrease the FWHM of the AOTF. In the limit when L approaches infinity the AOTF will only pass the specific wavelength that exactly satisfies the phase matching condition.

The peak (normalized) transmission on Equation (3.34) can be approximated by the value^[19,20]

$$I_o = \sin^2 \left(\frac{\pi^2}{2} \frac{M_2}{\lambda_o^2} \frac{P_a}{h} L \right)^{1/2} \quad (3.36)$$

where M_2 is the acousto-optic Figure of merit^[19] which relates the diffraction efficiency to the acoustic power for a given device geometry, h is the acoustic transducer height, P_a is the total acoustic power. A more exact expression for the intensity of the filtered light can be obtained from the coupled mode theory. The expression is^[19,20]

$$H(\lambda_o) = \pi^2 L^2 \eta^2 \text{sinc}^2[(\eta^2 + \Delta s^2)^{1/2} L] \quad (3.37)$$

where

$$\eta = \frac{1}{\lambda_o} \sqrt{\frac{M_2 P_a}{2 L h}} \quad (3.38)$$

The plane wave analysis described above can now be applied to an AOTF for an angular distribution of incident light. For a normalized light distribution $I(\Delta\theta$,

$\Delta\phi$), the transmission through the AOTF is obtained by integrating the plane wave response over the solid angular aperture^[17]

$$T(\lambda_o) = \int_{\Omega} H(\lambda_o, \theta_i, \phi_i) I(\theta_i, \phi_i) \sin\theta_i d(\theta_i) d(\phi_i) \quad (3.39)$$

where Ω is the solid angle.

3.3.2 AOTF Characteristics for Multiple Frequencies.

One of the most important characteristics of the AOTF is its multi-wavelength filtering capability. This is accomplished by having multiple RF frequencies going into the AOTF, each of these RF frequencies will filter the particular wavelength established by Equation (3.30). The number of simultaneous wavelengths that is possible to filter depends on the AOTF's RF drive power limitations and the power needed to filter each wavelength, given by Equation (3.36). But having multiple wavelengths in the AOTF will generate noise that might interfere with the measurements.

The presence of multiple frequencies in a Bragg cell will generate spurious intermodulation products (IMPs, combinations of signal frequencies) from the nonlinear response, which will result in signal degradation, for a more in depth analysis see reference [21]. The nonlinear response comes from multiple linear acousto-optic diffractions, acoustic and elasto-optic non-linearities^[21]. For example with N acoustic waves of frequency f_i (where $i = 1, \dots, N$) the total frequencies present will be

$$\sum_{k=-\infty}^{\infty} F_k = \sum_{i=1}^N m_{ki} f_i \quad (3.40)$$

where F_k would be the modes at the combination frequencies present in the medium, and m_{ki} are the weights of the particular frequencies (the weights may take any positive or negative integer number). The most important IMPs for two simultaneous signals (f_1 and f_2) are the two-tone, third-order IMPs that occur at the combination frequencies of $2f_1 - f_2$ and $2f_2 - f_1$ ^[21]. The IMPs due to sum or difference of the frequencies would lie outside the range of the AOTF. Under the assumption that multiple diffractions are possible, the magnitude of the two tone third order IMPs due to acousto-optic diffraction is given by^[21]:

where I_1 and I_2 are the fractional diffracted light intensities of the optical signals (Equation (3.34)). But in an AOTF multiple diffraction is not possible. The reason for this being that a second diffraction will not satisfy the phase matching conditions (Equation (3.30)), therefore it will not take place. The other source of non-linearity is the two-tone third-order IMPs due to acoustic and elasto-optic non-linearities whose magnitude is given by^[21]:

where β_1 and β_2 are the lowest order acoustic non-linear parameters, τ is the optical aperture in unit time, ρ is the mass density of the medium, V is the acoustic velocity, and $f = 2f_1 - f_2$ or $f = 2f_2 - f_1$ depending on which intermodulation product you desire to study. β_2 being a higher order is negligible except when β_1 vanishes (this occurs for shear modes propagating along principal axes^[21]). Equation (3.42) was obtained by making the assumption that a uniform optical beam was used.

3.3.3 Acousto-Optic Modulation.

The acousto-optic interactions can be used to modulate the signal going through the AOTF. In the AOTF, the maximum intensity of the filtered light is given by Equation (3.36). If the acoustic drive signal is amplitude-modulated, the intensity of the filtered optical signal will modulate. The peak optical intensity modulation will follow the formula:

$$H_o = \sin^2 \left(\frac{\pi^2}{2} \frac{M_2}{\lambda_o^2} \frac{P_a (1 + c_m \cos(\omega_m t))^2}{h} L \right)^{1/2} \quad (3.43)$$

Where c_m is the modulation index and ω_m is the modulating frequency. Only in cases when the acoustic power is small will the modulation in the optical signal follow the modulation in the acoustic signal. Otherwise the harmonics present in the modulation of the optical signal will be noticeable. Notice that the most important harmonics present are the second and third harmonics (i.e., $2\omega_m$ and

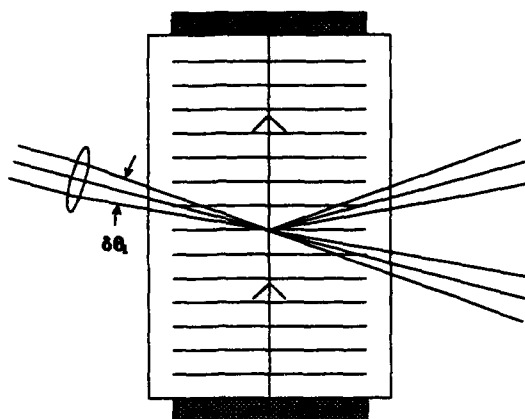


Figure 3.7. Acousto-optic modulation.

$3 \omega_m$).

The maximum modulation frequency of an acousto-optic Bragg device is inversely proportional to the amount of time that the acoustic wave takes to pass through the diameter of the finite optical beam, this is referred to as the transit time (or optical aperture in unit time) and is given by:

$$\tau = D/V \quad (3.44)$$

where D is the diameter of the optical beam, and V is the acoustic velocity. Notice that the maximum modulation frequency is also inversely proportional to the diameter of the optical beam^[22]. Therefore to increase the maximum modulation frequency the optical beam needs to be decreased by using a focusing lens. But this in turn causes an angular spread of the incident angle, $\delta\theta_i$ (see Figure 3.7). This angular spread must satisfy the law of conservation of momentum in all the directions, meaning that $\delta\theta_i$ must be within the angular aperture of the AOTF^[23]. If $\delta\theta_i$ is larger than the optical aperture of the AOTF then

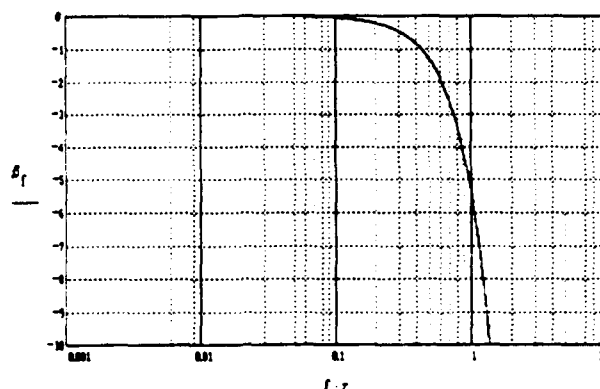


Figure 3.8. Modulation frequency response for analog acousto-optic modulation.

efficient Bragg diffraction will not take place for all the incident rays.

An acousto-optic Bragg cell in an amplitude modulation configuration will act as a low pass filter. Assuming a Gaussian input beam^[23], the frequency response in dB is given by:

$$\beta_f = 10 \log\left(\exp\left(\frac{-\pi^2 f^2 \tau^2}{8}\right)\right) \quad (3.45)$$

Figure 3.8 illustrates Equation (3.45), note that at $f\tau = 1$ the modulation amplitude has been reduced considerably. Using Equation (3.44) the relationship between the beam width and the modulation frequency can be obtained^[23].

3.4 Acousto-Optic Tunable Filter - Fiber-optic Brag Grating system

In this section a theoretical analysis of the Acousto-Optic Tunable Filter - Fiber-optic Brag Grating (AOTF-FBG) system will be made, later Chapter 4 will describe the actual setup and results. The system under consideration will utilize

an AOTF as a high speed spectrum analyzer. Figure 3.9 illustrates the AOTF-FBG system configuration. The light coming out of the FBG sensor embedded fiber will enter the AOTF, where it will be analyzed. As it was shown in the last chapter, the center wavelength of the optical passband is determined by the acoustic RF frequency. The RF frequency can be swept so that the center wavelength of the passband sweeps within the range of the FBG sensor. Depending on the mode of operation of the sensor (reflection or transmission), the Bragg wavelength can then be determined by determining the RF frequency where a maximum or minimum occurred. Using the unique ability of the AOTF

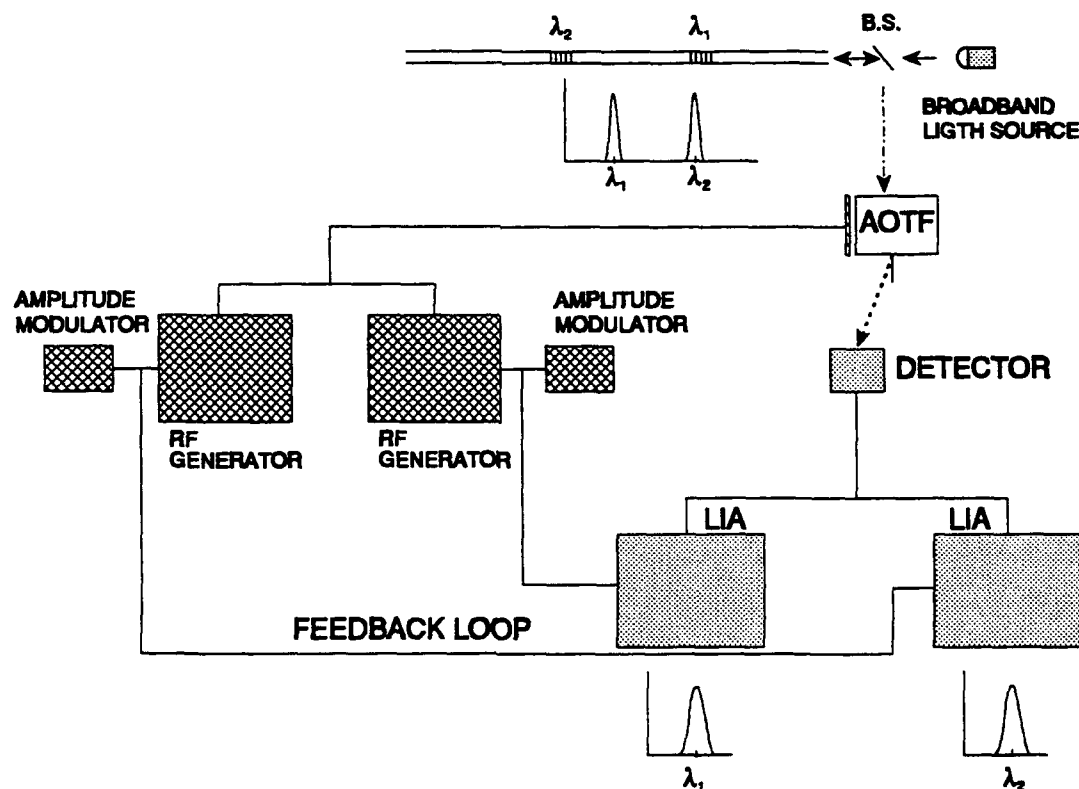


Figure 3.9. AOTF-FBG system configuration for a two-channel sensor fiber.

to simultaneously filter multiple wavelengths, multiple sensors can be interrogated simultaneously. This capability will prove useful in increasing the system speed. Another capability is utilizing a single detector to monitor all the channels, this is what it is going to be done in this system. Each channel will be amplitude modulated and then electronically filtered to separate the signals coming from them. This process will definitely produce noise. In this section the noise due to the acousto-optics interactions will be analyzed.

3.4.1 Analysis of Multiple Frequencies Present on an AOTF.

When more than one frequency is present in the AOTF, inter-channel crosstalk due to the sidelobes of the bandpass becomes present. The amplitudes of the bandpass sidelobes for a single channel with an efficiency of 95% ($M = 1.07323 \times 10^{-13} \text{ s}^3/\text{Kg}$, $P = 500 \text{ mW}$) are illustrated on Figure 3.10, where the amplitude α is given in dB and the FWHM for this filter is 0.74 nm. The attenuation between the main lobe and the side lobes is dependent on the maximum efficiency of the bandpass and is approximately given by:

$$\frac{I_{\text{sidelobe}}}{I_{\text{max}}} \approx \left[\frac{2 \eta L}{(2n+1) \sin(\pi L \eta)} \right]^2 \quad (3.46)$$

where $n = 1, 2, \dots$ is the sidelobe order, absolute value. The minimum separation for the Bragg sensors is 5 nm, this is assuming a tuning range of 4 nm and a 1 nm spacing between channels. Due to the bandwidth and power limitations of solid state optical sources, the channels need to be placed as close as possible.

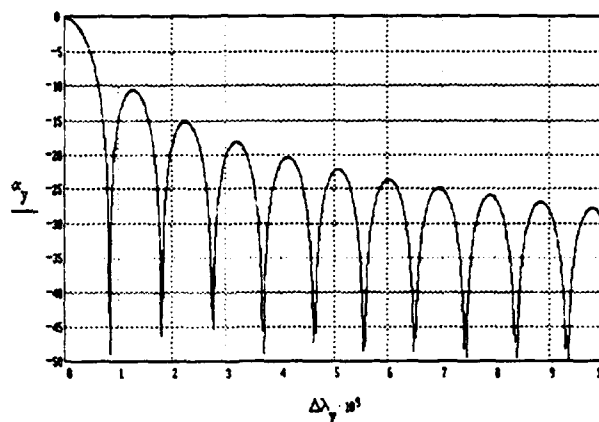


Figure 3.10. Single channel bandpass levels for an ideal AOTF centered at 833 nm using a TeO_2 crystal.

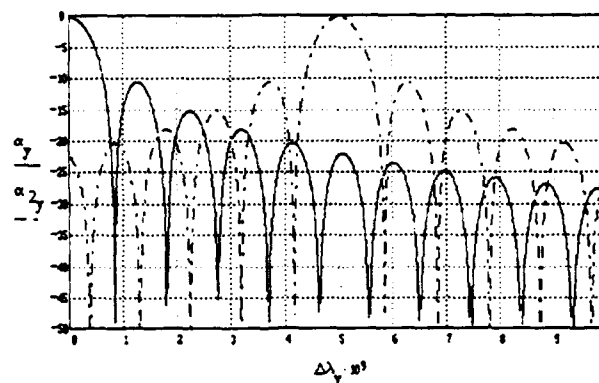


Figure 3.11. Multiple channels bandpass levels for an ideal AOTF, at 833 and 838 nm using a TeO_2 crystal.

With this in mind, the separations between channels will be 5 nm. One way to reduce crosstalk is to make the center wavelengths of the AOTF be separated by the channel distance, 5 nm, at all times, i.e., the channel sweep will be done in a synchronized fashion. Figure 3.11 shows the sidelobes intensity levels for a two channel AOTF, this separation should be maintained at all times for minimal interference. If in addition to that, each signal is amplitude modulated and then electronically filtered using a Lock-In-Amplifier (LIA), the inter-channel crosstalk

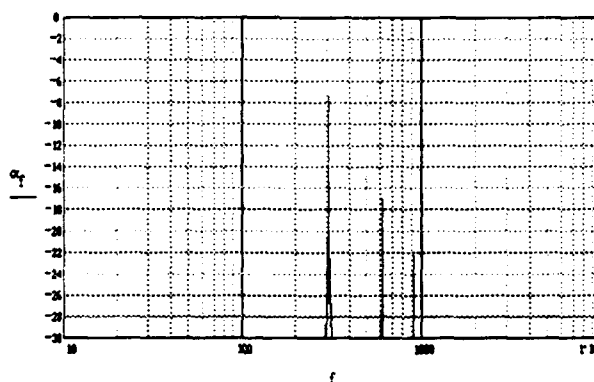


Figure 3.12. Frequency characteristics of Equation (3.43) with $\omega_m = 2\pi * 300$ Hz, amplitude is in dB.

would be greatly reduced (most of the reduction would come from amplitude modulation). Amplitude modulation is not free from harmonics. Figure 3.12 shows the AM frequency domain characteristics for an ideal TeO_2 AOTF with $M_2 = 4.65597 * 10^{-14} \text{ s}^3/\text{Kg}$, $L = 19 \text{ mm}$, $P_a = 200 \text{ mW}$, and $\lambda = 833 \text{ nm}$ (the bandpass has a 28% efficiency with the maximum sidelobes being 13 dB below the main lobe). As mentioned in Section 3.2.3, second and third harmonics are present, but the LIA in bandpass mode could be selective enough to attenuate these harmonics. The problem would be on how close, in the frequency domain, the two AM signals can be placed before interfering with each other, this should be very close since the LIA also locks in phase. Even with a 100% separation between channels, in the worst case scenario, there would be a signal-to-noise ratio (SNR) of about 10 dB, depending on the efficiency of the AOTF (Equation (3.46) with $n = 1$, first order). This would take place when the Bragg wavelength of the sensor of the adjacent channel is at its maximum (minimum) value and that of the present channel at its minimum (maximum) value. An alternative would be

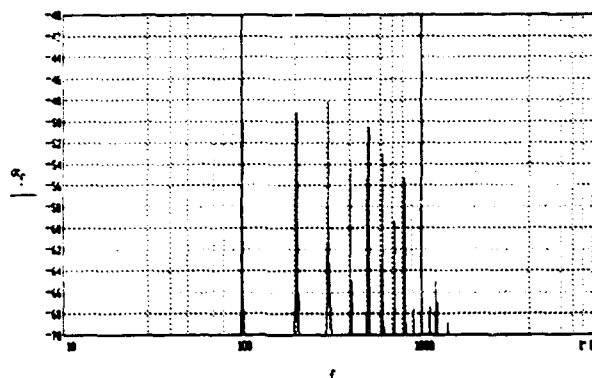


Figure 3.13. Frequency characteristics of Equation (3.42) with $f_1 = 300$ Hz and $f_2 = 200$.

to use sidelobes suppression techniques as described on reference [24]. One problem with these techniques is the broadening of the FWHM of the passband. Another possibility is to reduce the bandwidth of the AOTF's bandpass.

Other sources of noise are the intermodulation products (Section 3.3.2) whose intensities are given by Equation (3.42). The AM frequency domain of Equation (3.42) is given in Figure 3.13, the second term of the equation is being neglected. The same parameters from Figure 3.12 were used plus $\lambda_2 = 838$ nm, $\tau = 21$ μ s, $V = 914$ m/s, and $\beta_1 = 1$. The actual value of β_1 will play an important role in determining the amount of noise coming from the IMPs. Amplitude modulation, along with electronic filtering, can reduce considerably the amount of crosstalk between channels, but it will not guard against the noise coming from the same channel.

3.4.2 Sweep Analysis

The sweeping action of the AOTF's bandpass, along with the detector, creates a convolution process between the sensor signal and the bandpass. Figure 3.14 illustrates the reflection of a FBG (1.0 would be 100 % efficiency) with a FWHM of 0.1 nm. Since the reflection has a much smaller bandwidth (about a factor of 7.4 smaller) than the AOTF's bandpass, using the same parameters for the AOTF that were used for Figure 3.12, their convolution will give us almost the same function as that of the AOTF's. Let's take two adjacent Bragg sensor channels, each with a tuning range of 4 nm and a 1 nm separation, and have center frequencies of 833 and 838 nm. If the Bragg wavelength of one channel is at 835 nm (maximum) and the other at 836 nm (minimum) then there will be a deviation of 0.05 nm from the real value, this can be seen on Figure 3.15. The reason for this deviation is that the first sidelobe of the bandpass is able to reach the minimum values of the adjacent channel. This interference will create the shift in wavelength of the convolution of the signal at the maximum values. If the

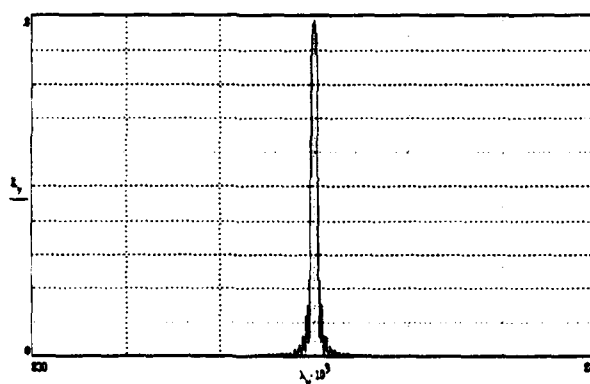


Figure 3.14. Ideal reflection of a FBG, Equation (3.2), with a FWHM of .1 nm.

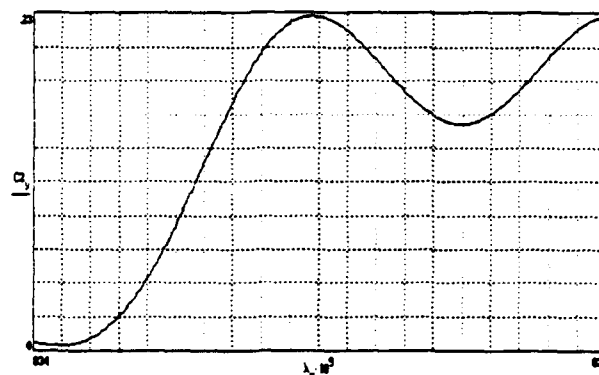


Figure 3.15. Convolution between the FBG function (Equation (3.2)) and the ideal AOTF function.

separation between channels is increased to 1.6 nm the deviation reduces to 0.0165, this one is due to interference coming from the first and second sidelobes. If precision greater than this is necessary it is suggested that the bandpass of the AOTF be decreased as much as possible, without sacrificing efficiency. Another alternative is to implement sidelobe suppression^[24] along with bandpass reduction.

4. EXPERIMENTATION

4.1 Experiment set-up

This section outlines the experimental setup, the equipment and the procedure of the experiment. Figure 4.1 shows the schematic diagram of the experimental setup. Note the difference between Figure 4.1 and Figure 3.9, Figure 4.1 is the actual experimental setup after the substitution of the broadband light source with the two lasers. The broadband light source didn't have the sufficient power nor did the detector have the sensitivity enough to overcome the losses of the system.

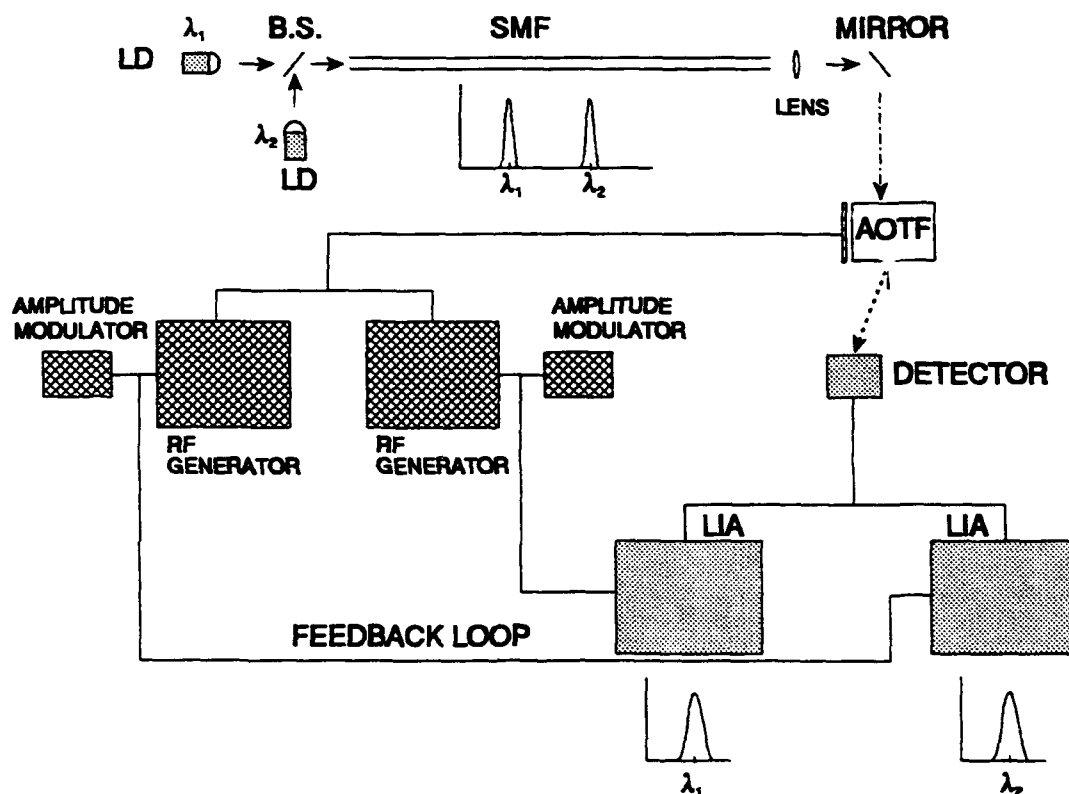


Figure 4.1. Schematic set-up of experiment.

The two reflected signals from the sensors can be simulated by using a pair of lasers. The laser's output is very similar to the FBG output. The difference is in the amount of optical energy available. The Laser diodes (LD), the single mode fiber (SMF), the AOTF and the detector were mounted on an optical rail system for ease of alignment and to secure the setting once the alignment is done.

The lasers used were both semiconductor lasers, Spectra Diode Labs 100 mW GaAlAs laser diode model SDL-2410 and the other was a Sharp model LTO15MD, both lasers were temperature controlled. A beam splitter was used to combine both beams in the same direction. To couple the light into the fiber a Newport single mode fiber positioner F-916 series was used. Once the light goes out of the fiber it is collimated with a lens and fed into the AOTF, the AOTF's specifications measured and given by the manufacturer, Aurora

Table 4.1. Specifications of the AOTF

Spectra Bandwidth @ 633 nm	0.31 nm
Wavelength range	0.7 - 1.5 μm
Optical aperture	1 mm
Deflection angle	> 3°
Efficiency	- 75%
RF input frequency	50 - 200 MHz
Random Access time	1 μsecond
Input impedance	50 Ω
VSWR	2:1

Associates are given on table 4.1. The AOTF will filter the corresponding wavelengths into the detector. The AOTF is placed after the fiber to assure that the entrance angles of both lasers are the same.

The two LIA will separate the signals and display their intensities. A computer will be attached to the LIAs and the RF generators to record the data. The LIAs are Princeton Applied Research LIA model 124A and have preamplifier modules 118 and 185. The RF generation is being done by two RF generators, one for each channel. One of the generators is a sweep generator from HP model 8350B with a HP83525A plug-in, the second generator is alternated between a CW generator (not a sweeper) HP8640B and a sweep generator HP8620C with a HP86222B plug-in. The second generator is alternated because the HP8640B has an almost negligible drift in frequency (along with digital readouts) while the HP8620C has a very noticeable drift, this one was only used to scan both channels simultaneously. The amplitude modulators are normal signal generators used in the laboratories (e.g., Wavetec model 142).

The experiment will consist of first making an optical spectrum analysis of the laser diodes and the AOTF's bandpass. This will be done with a SPEX model 1269 1.26m monochromator with a readout accuracy of < 0.05 nm and Spex DM-3000 controlling software. Then an RF spectrum analysis of the RF signals going into the AOTF will be made. Once these measurements are done and the components are installed and aligned, a series of experiments will be made in which one of the AOTF's bandpass will scan the region where just the wavelength

of one of the lasers is located, simulating thus a channel sweep of a sensor. While the other AOTF's bandpass will remain fixed at the second laser's wavelength. At first the modulating frequencies of the RF signals will be 100 Hz and 300 Hz. In successive tests the 100 Hz modulation will be increased to see the effects on the signal acquisition. Finally the two bandpasses will be made to scan their respective lasers.

4.2 Recorded Data and Observations

A Super Radiant Diode was used for the broadband source. The power available for the silicon detector after coupling to the SMF (Single Mode Fiber) and filtering was too small to prevent its detection. Also, the output of the two lasers is very similar to the output of the FBG, but with higher power. The result of the experiment won't be affected by this change. For this reason the Bragg gratings were substituted for two laser beams at slightly different frequencies. Early during the experiments it was noted an amplitude frequency relation that didn't follow Equation (3.45). To study the exact relation, a single RF frequency with a square wave amplitude modulation was applied to the AOTF. Figure 4.2 illustrates a photograph taken to the oscilloscope trace. From the curve it was

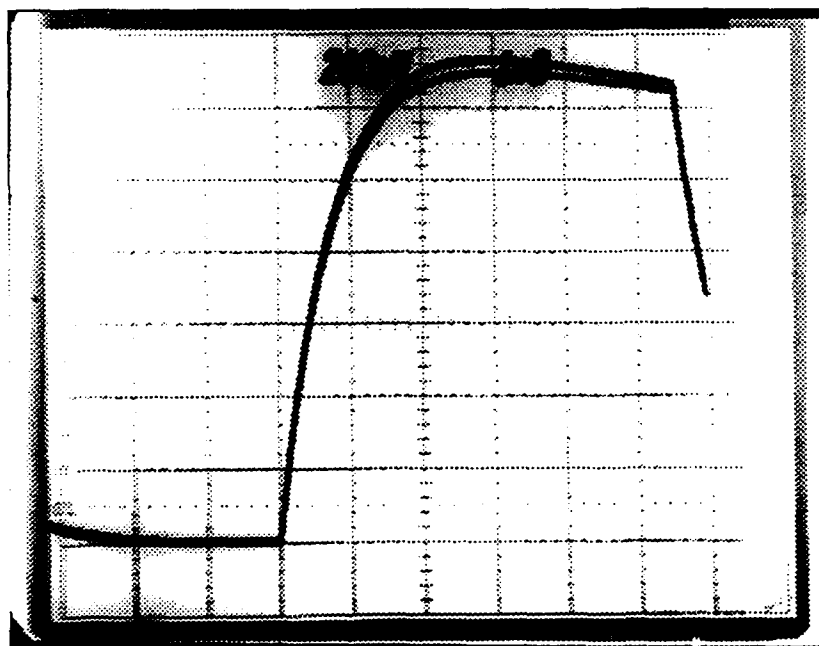


Figure 4.2. AOTF's filter response of a square wave amplitude modulation. The scales are 200 $\mu\text{V}/\text{div}$ and 1 ns/div.

speculated that the AOTF used in the experiment was of a resonating type^[24], and thus would behave as a low pass filter for amplitude and frequency modulation.

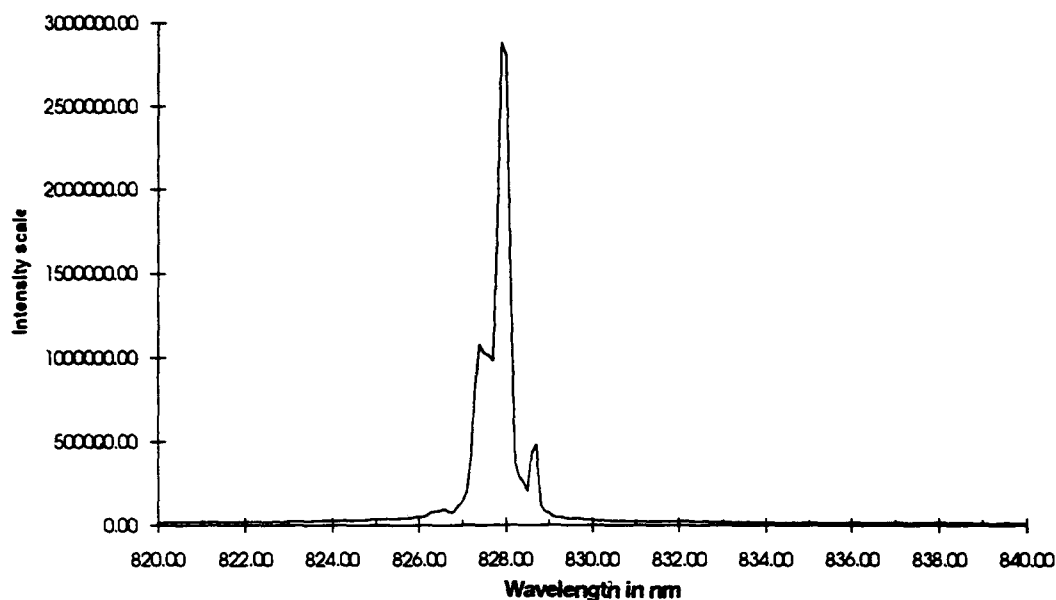


Figure 4.3. Spectra Diode Labs Laser model SDL-2410.

Figure 4.3 shows the spectrum of the Spectra Diode Labs laser. This laser has a FWHM of approximately 0.35 nm with the peak wavelength being at 827.9 nm. The data was taken at 0.1 nm intervals. The laser were set to a temperature of 19.6°C, current was set to 273 mA, and the power was at 55 mW. In order to measure the light of the laser diode it had to be attenuated because of saturation problems in the detector. These measurements took approximately 3.5 minutes to obtain with a 1-second integration time.

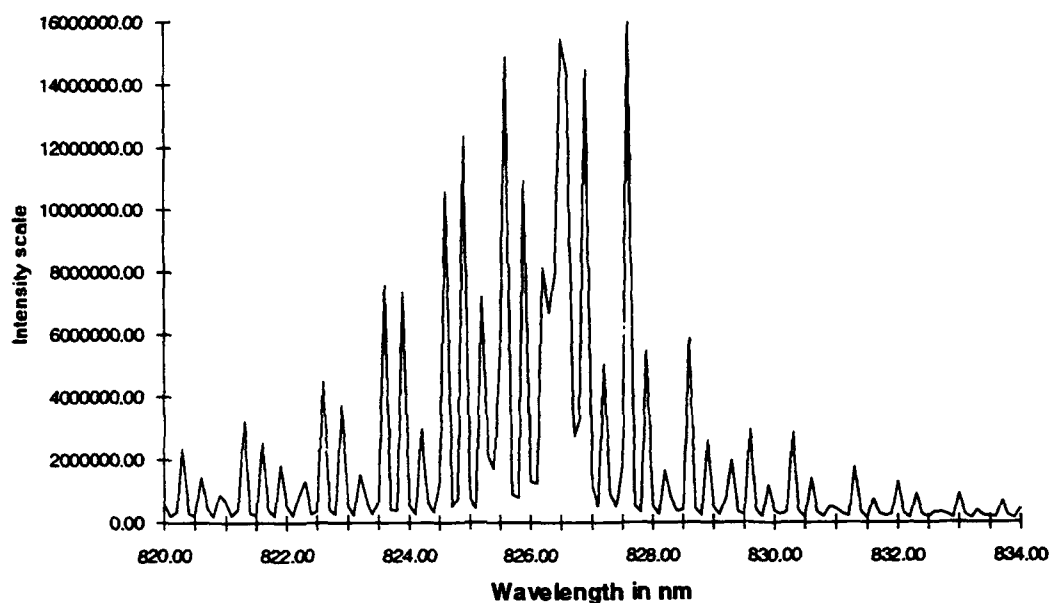


Figure 4.4. Optical spectrum of Sharp's laser diode model LTO15MD.

The Sharp's spectrum is illustrated on Figure 4.4. This spectrum was taken after the scanning experiment were made (a few months later). It is thought that the Laser diode degraded. Some of its parameters will have to be inferred from the experimental data. The Laser was driven at 60.1 mA and the thermocouple had an ohmic resistance of 10.59 (about 24.2 °C). Previous measurements place the center wavelength around 825 - 826 nm.

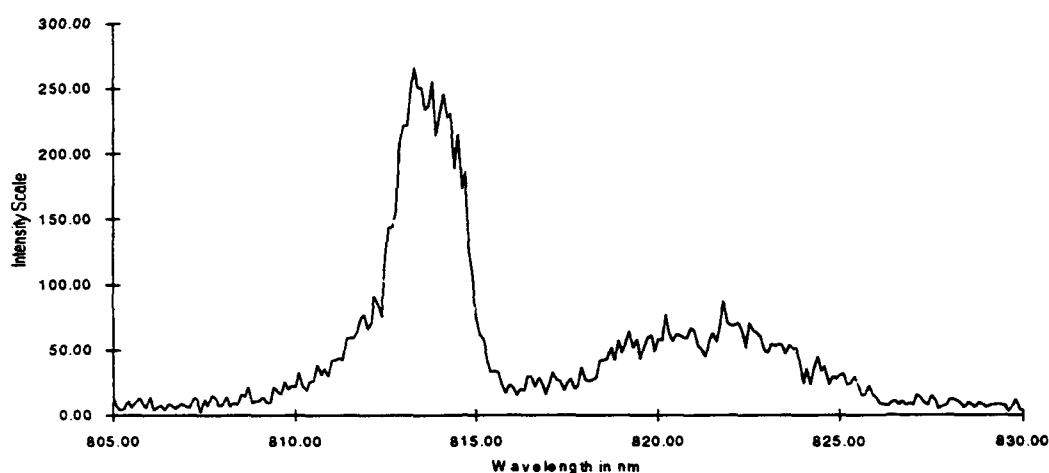


Figure 4.5. Bandpass of the AOTF.

Figure 4.5 shows the optical bandpass of the AOTF used in the experiment. All the experimental measurements were done with this device. This bandpass meets the output specifications of the manufacturer. The only difference would be higher crosstalk due to the sidelobes when the two optical signals are close wavelength. The frequency used was 153.102 MHz. The RF signals were set to ≈ 400 mW. The sampling interval was 0.1 nm. For this measurement the Broadband optical source was a SMF pig tailed super luminescent diode from Laser Diode, Inc., model SRD-8300. The FWHM for this plot was approximately 2.3 nm and the center wavelength was 813.3 nm.

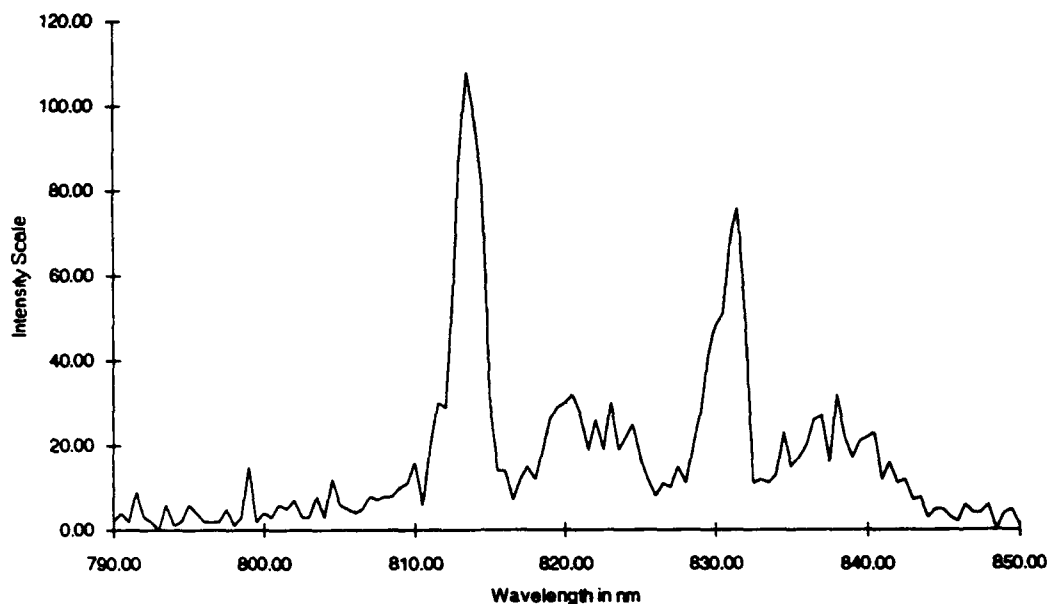


Figure 4.6. Bandpass of the AOTF with two RF frequencies.

Figure 4.6 shows the optical bandpass of two simultaneous RF frequencies being fed to the AOTF. The frequencies used were 153.102 MHz, for the lower wavelength, and 149.538 MHz, for the upper wavelength. Both RF signals were set to ≈ 180 mW of power. The sampling interval was 0.5 nm. For this measurement the Broadband optical source was the SRD-8300.

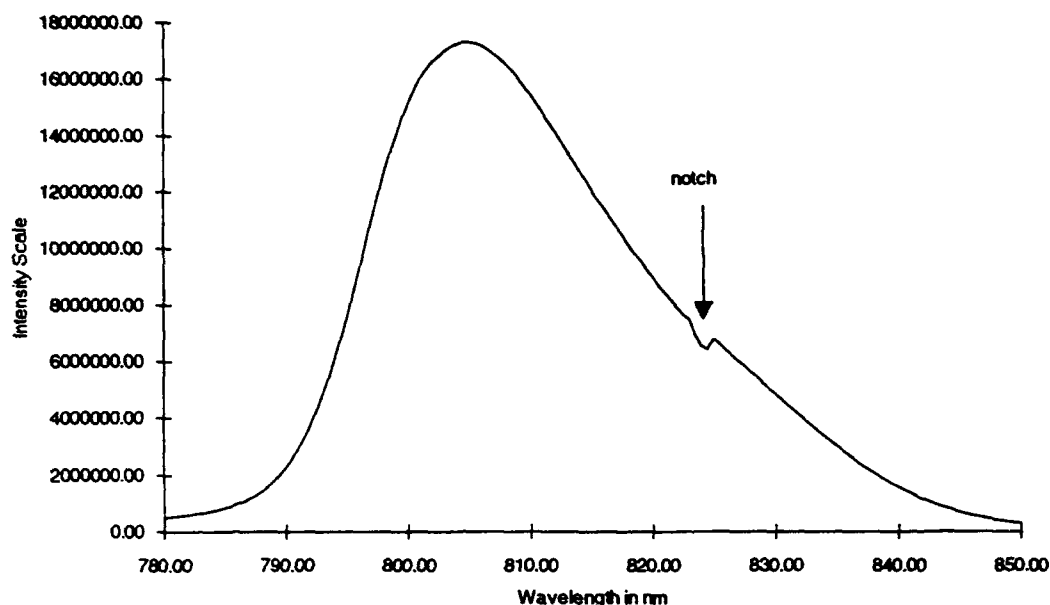


Figure 4.7. SRD-8300 spectrum when passing through the FBG.

Figure 4.7 shows the spectrum of the SRD-8300 as it comes out of the FBG sensor embedded fiber. Notice the notch is very small in width and amplitude. This is due to the fact that spectral scanning is a convolution between the bandpass and the signal. For us to observe a small but wide notch is an indication that the bandpass is larger than the optical signal. The measurements were taken every 0.5 nm apart. This might be one of the causes. Notice that the AOTF's bandpass amplitudes on Figure 4.6 follows the shape of this plot.

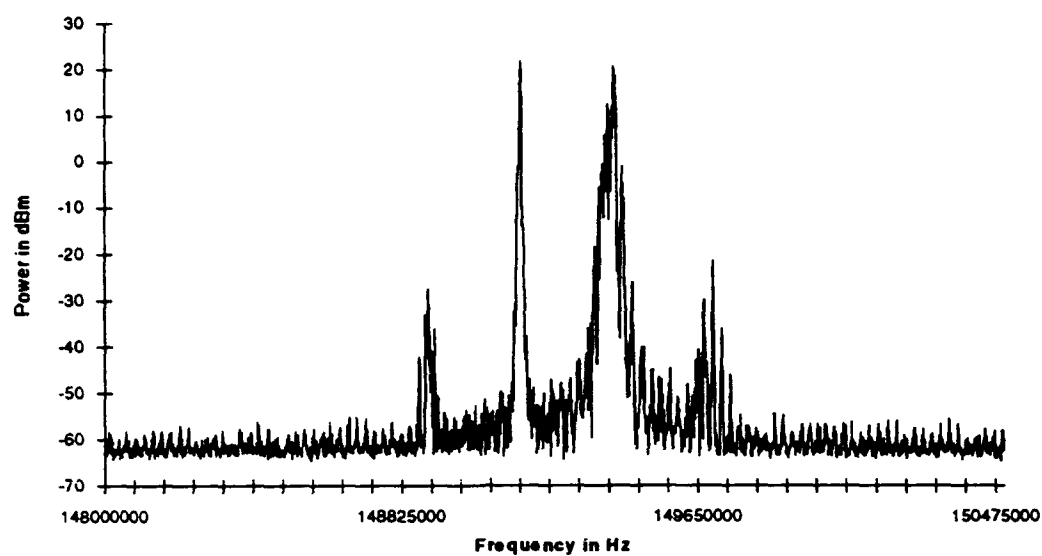


Figure 4.8. RF spectrum of two oscillators. A fix oscillator was set to 149.157 MHz and 300 Hz AM and a sweep oscillator was set to a fixed frequency of 149.410 MHz and 100 Hz AM.

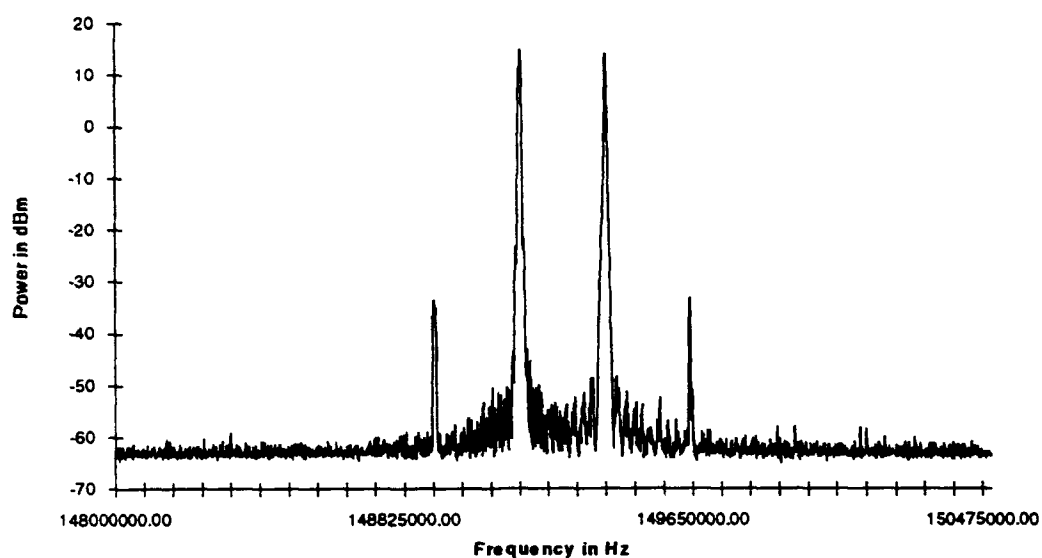


Figure 4.9. RF spectrum of two oscillators. One fix oscillator was set to 149.157 MHz and 300 Hz AM and a second fix oscillator was set to a frequency of 149.4025 MHz and 100 Hz AM.

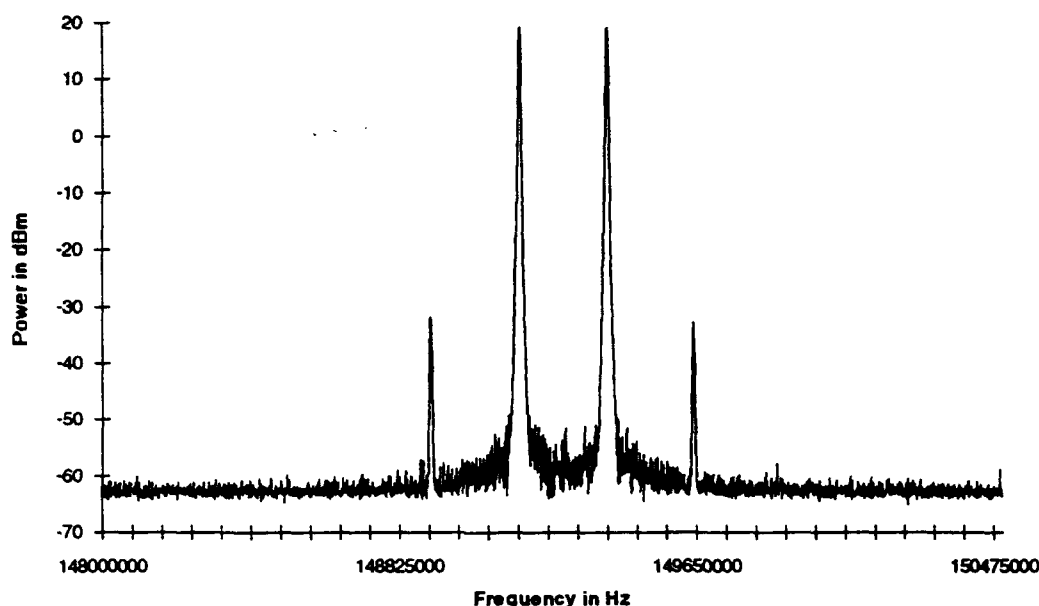


Figure 4.10. RF spectrum of two oscillators. One fix oscillator was set to 149.157 MHz and a second fix oscillator was set to a frequency of 149.4025 MHz. No modulation was used.

The three previous figures show the RF spectrum of the frequency generators after a two signal mixing. Figure 4.8 shows two mixed signals and their respective harmonics. One of the RF generators was a fixed (CW, not capable of frequency scanning, HP8640B) and the other was the frequency sweeper (HP8620C). Both of these signals were amplitude modulated. Note that the continuous wave signal has a smaller bandwidth than the sweeper signal. Having a broader RF bandwidth could increase the bandwidth of the AOTF's optical bandpass for the scanning signal. Figure 4.9 is similar to Figure 4.8 except that both signal generators are fixed (i.e., CW). Figure 4.10 has the same configuration as Figure 4.9 except that the signals are not being amplitude modulated.

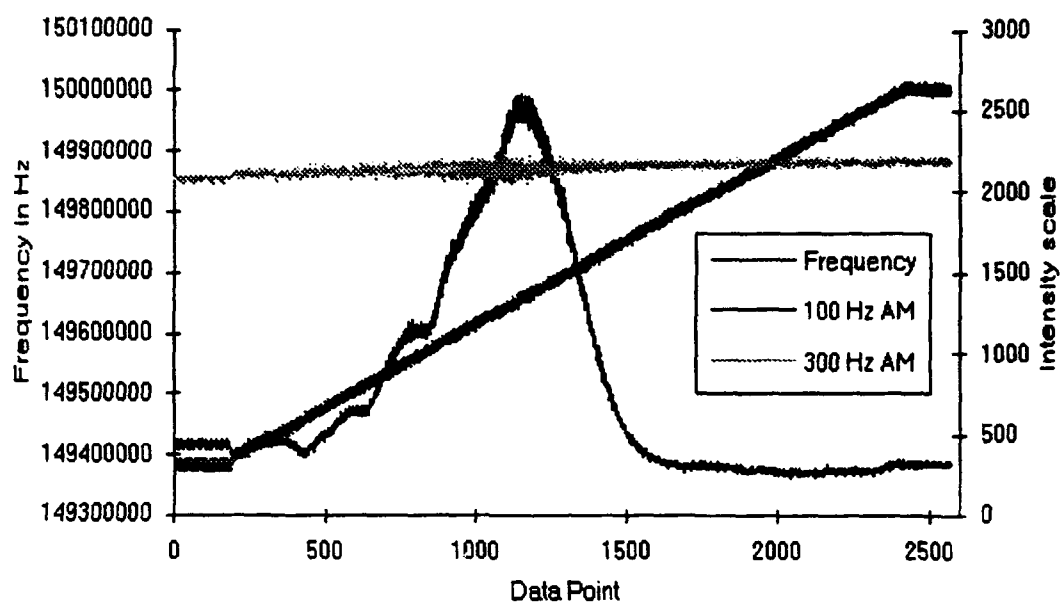


Figure 4.11. Data taken with sinusoidal amplitude modulation. Intensity scale is 1 mV/4095.

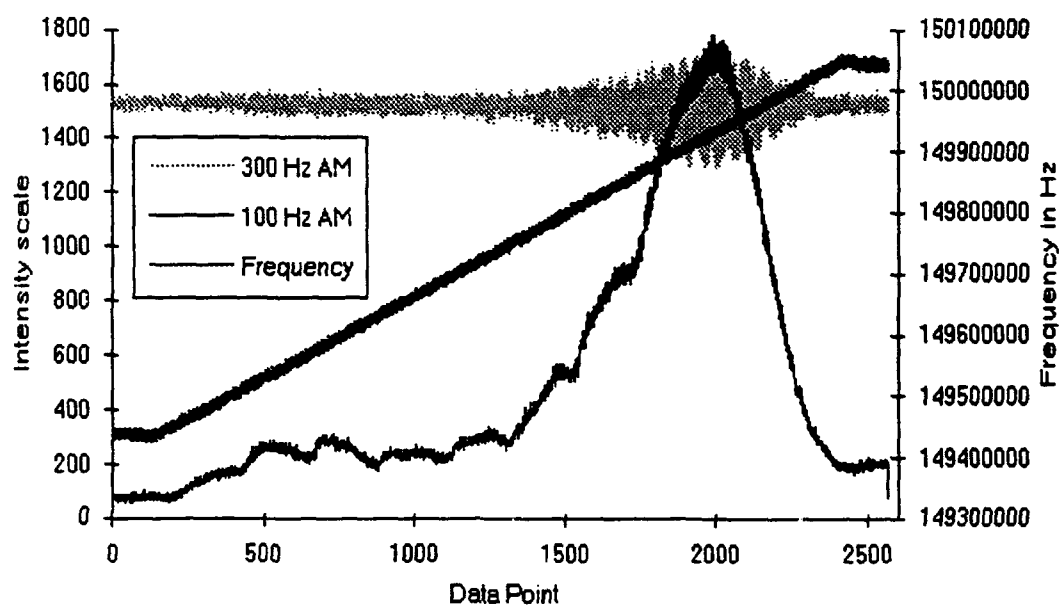


Figure 4.12. Data taken with a square wave amplitude modulation. Intensity scale is 1 mV/4095.

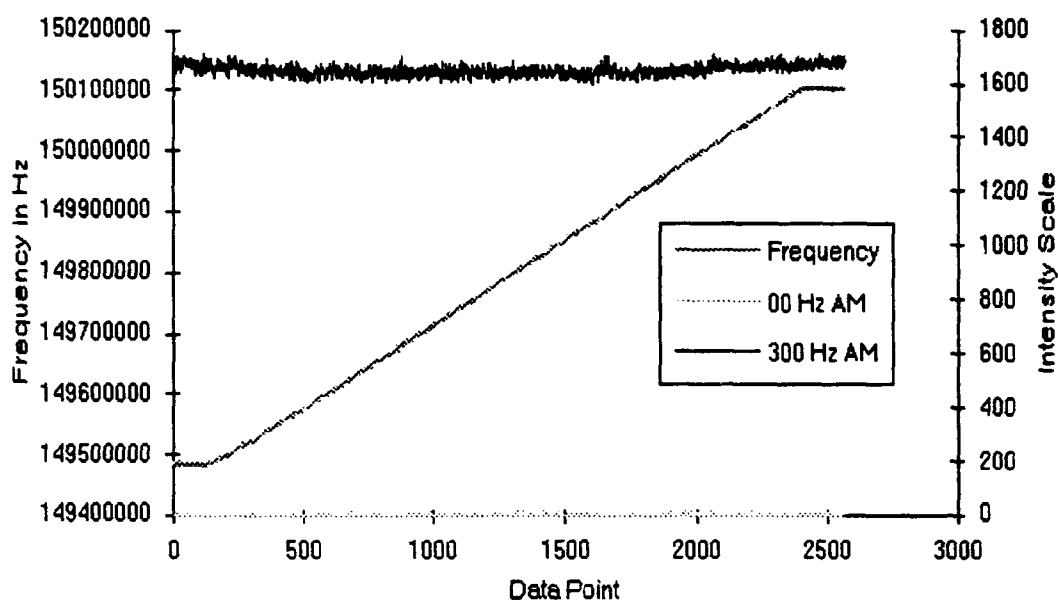


Figure 4.13. Data taken with a square wave amplitude modulation on only one channel. Intensity scale is 1 mV/4095.

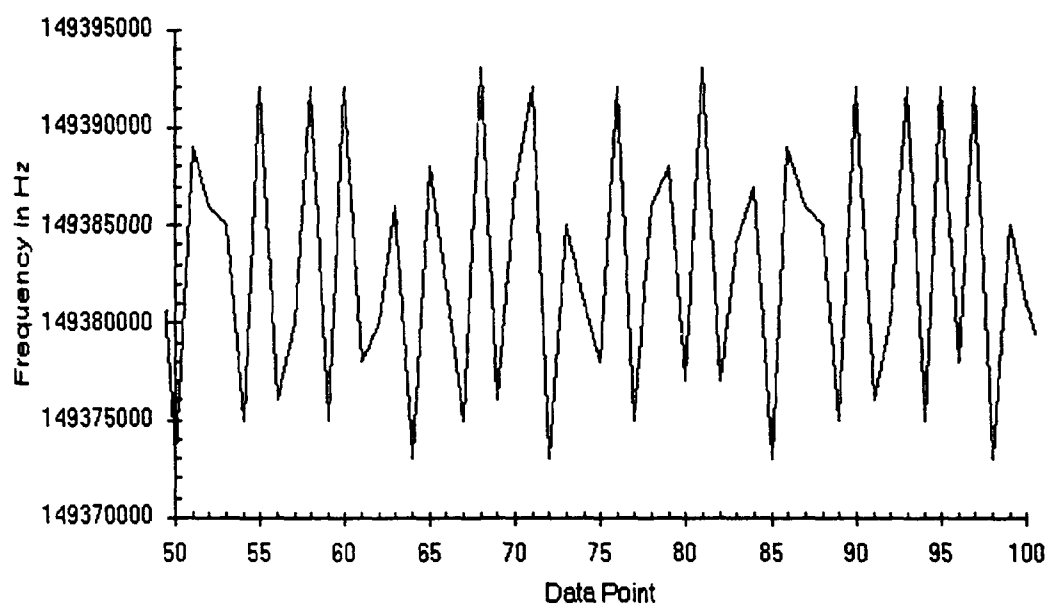


Figure 4.14. Amplification of the frequency plot in Figure 4.11.

On Figures 4.11 - 4.13 the data tagged "Frequency" correspond to the output of the RF frequency sweeper, it is sweeping a frequency region, and its amplitude is read on the frequency axis. The amplitude of the modulated signals are tagged with their corresponding AM frequency, these conventions will be maintained throughout the rest of the data plots. Figures 4.11 and 4.12 are experimental data taken using 100 Hz and 300 Hz amplitude modulation. In Figure 4.13 only one of the signals was amplitude modulated, but both RF signals were present (The LIA was not adjusted to follow the 0 Hz signal). The LIAs were set at the 1 mV scale and a Q of 10 (see appendix A). The output of each RF signal generator was set to 100 mW. The Spectra Diode Labs (SDL) laser was monitored by the fixed RF generator which had an AM signal of 300 Hz and an RF signal of 149.168 MHz. The Sharp's diode was monitored by the sweep generator, 100 and 00 Hz. In these plots the frequency data are not used to label the X-axis because it has an oscillating period consisting of two or more low frequencies with a peak to peak width of 20 KHz for Figures 4.11 and 4.12 and 5 KHz for Figure 4.13. Figure 4.14 illustrates the oscillating motion of the frequency plot. It was determined that the RF sweep generator was generating the oscillations, the CW RF generator wasn't contributing any oscillation. Each data point was taken at an interval of approximately 0.045 sec. Notice that there is an increase in the oscillation amplitude of both signals in Figure 4.11, and even more in Figure 4.12, as the intensity of the swept signal increases.

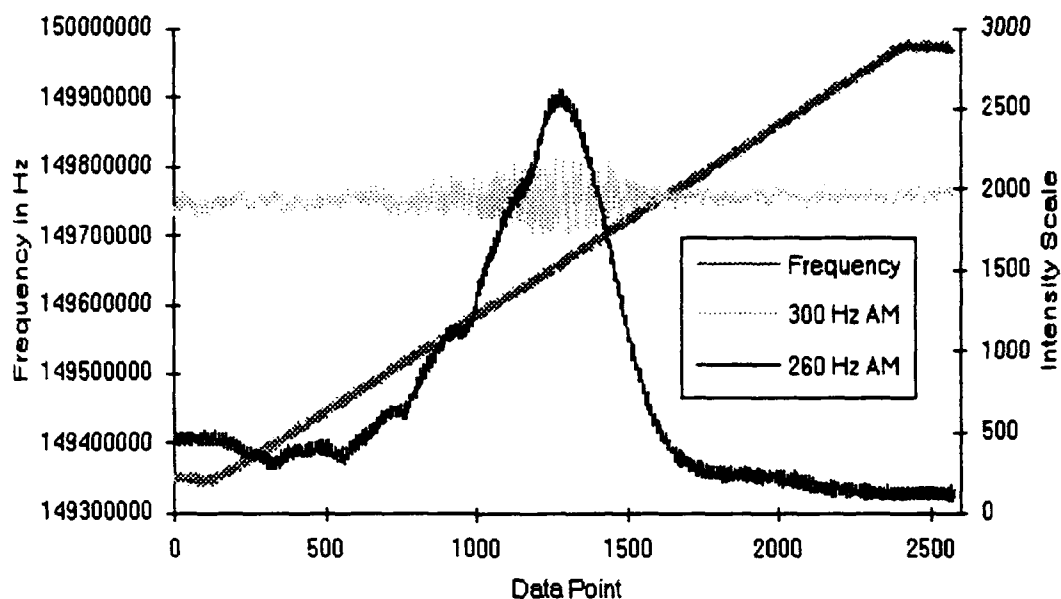


Figure 4.15. Sweep plot with sinusoidal amplitude modulation. Intensity scale is 1 mV/4095 for the 300 Hz and 2 mV/4095 for the 260 Hz signal.

Figure 4.15 shows a plot of experimental data taken with the amplitude modulation of both signals being separated by just 40 Hz. The RF sweeper is used for the 260 Hz AM signal while the fixed RF generator is being used for the 300 Hz AM signal. The p-p amplitude of the frequency's oscillation is approximately 13-15 KHz. Notice that the p-p amplitude of the signal's oscillation, when both signals are at maximum, is greater for this reduced separation. In this experiment the LIAs were set at $Q = 10$ and the RF signal generators were set at 100 mW output and the fixed (CW) generator was set to 149.249 MHz.

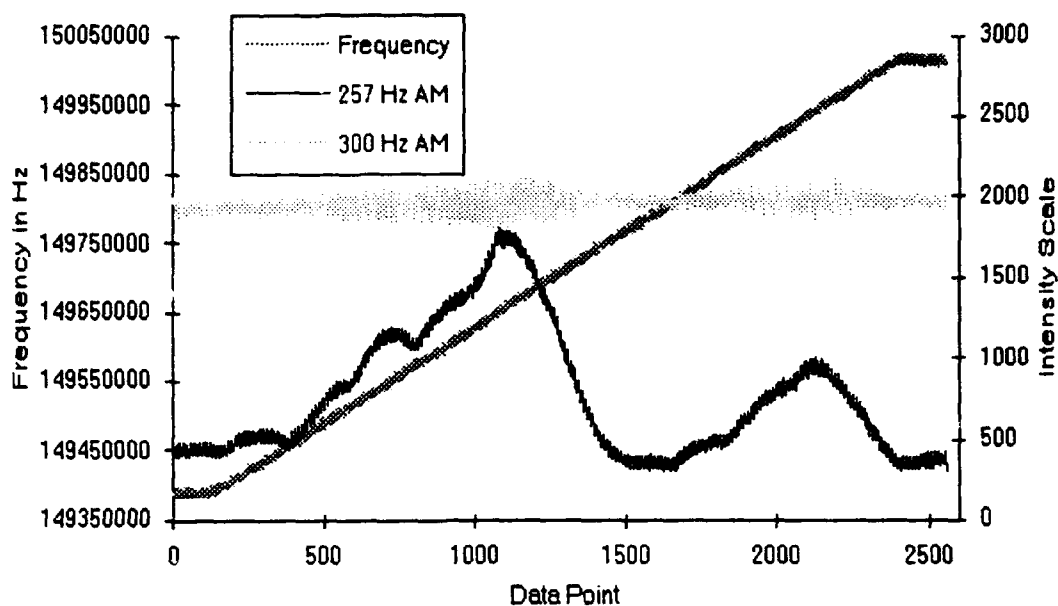


Figure 4.16. Data showing a wavelength transition in the Sharp's diode. Sinusoidal amplitude modulation and the intensity scale is 2 mV/4095 for the 257 Hz and 1 mV/4095 for the 300 Hz signal.

The parameters in Figure 4.16 are the same as in Figure 4.15. Figure 4.16 shows a wavelength transition of the Sharp's laser diode (i.e., changing the wavelength of the output energy). Note that only the 257 Hz signal is changing meaning that it's a change in the laser diode and not in the AOTF. The SDL laser changes also the wavelength of its peak output but at longer time intervals. This demonstrates the instability of the lasers and also the ability of the AOTF to detect the change in wavelength.

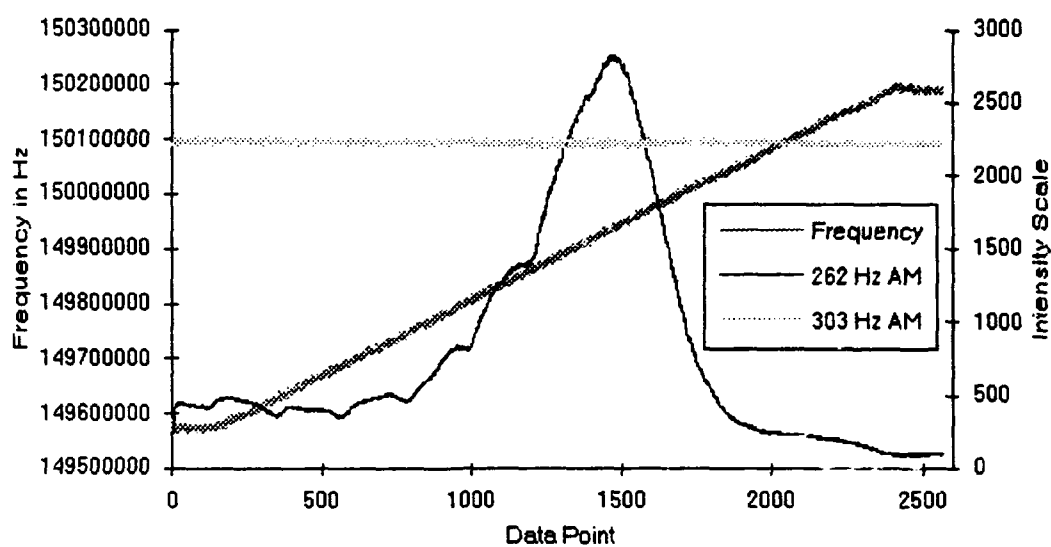


Figure 4.17. Wavelength scan on the Sharp's laser diode with a sinusoidal AM. LIA was set at $Q = 100$, the intensity scale is 1 mV/4095 for the 303 Hz and 2 mV/4095 for the 262 Hz signal.

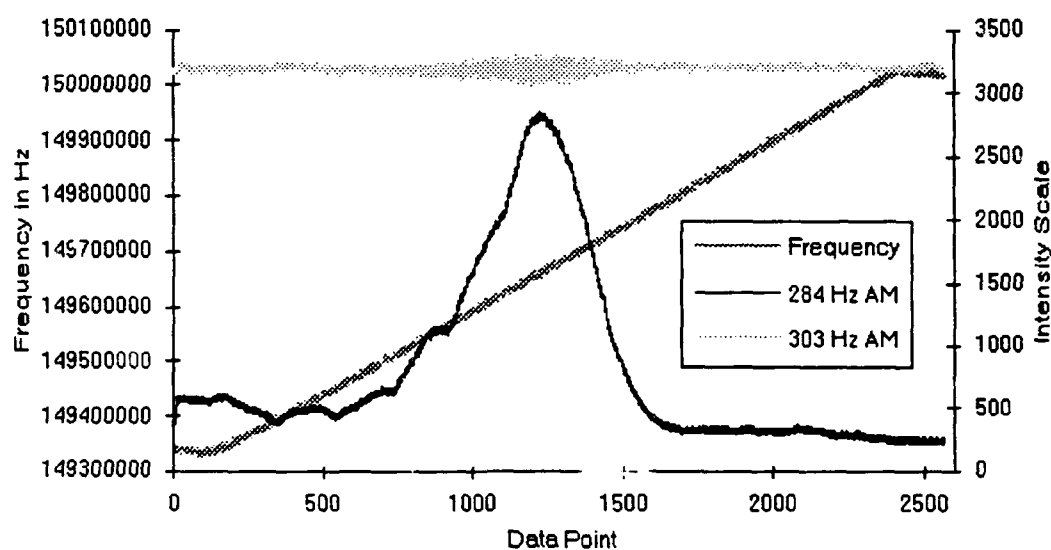


Figure 4.18. Wavelength scan on the Sharp's laser diode with a sinusoidal AM. LIA was set at $Q = 100$, the intensity scale is 1 mV/4095 for the 303 Hz and 2 mV/4095 for the 284 Hz signal.

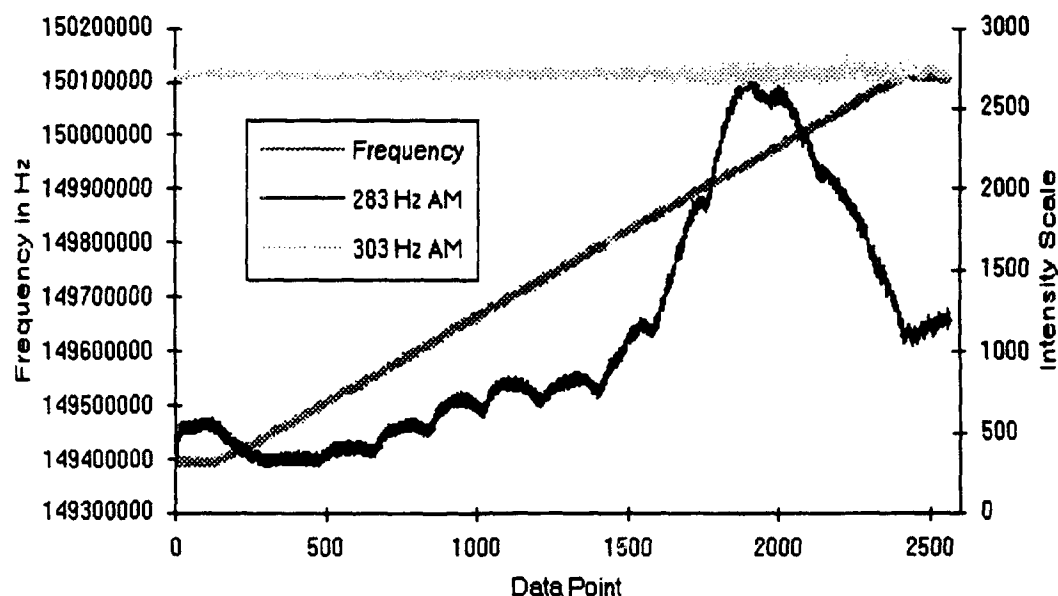


Figure 4.19. Wavelength scan on the Sharp's laser diode with a square wave AM. LIA was set at $Q = 100$, the intensity scale is 1 mV/4095 for both signals.

The plots on Figures 4.17, 4.18, and 4.19 were made with the LIAs set at $Q = 100$. The RF sweeper is used for the 262, 284, and 283 Hz AM signals while the fixed generator is being used for the 303 Hz AM signal. Notice that the amplitude of the oscillations (noise) have been greatly reduced. Even the 20 Hz separation between the signal of Figure 4.18, with a square wave modulation, has less noise than the plot on Figure 4.15, 40 Hz separation and sinusoidal AM. The CW generators on Figures 4.17, 4.18, and 4.19 had a frequency of 149.249, 149.242, and 149.216 MHz, respectively, and their individual power output was set to 100 mW.

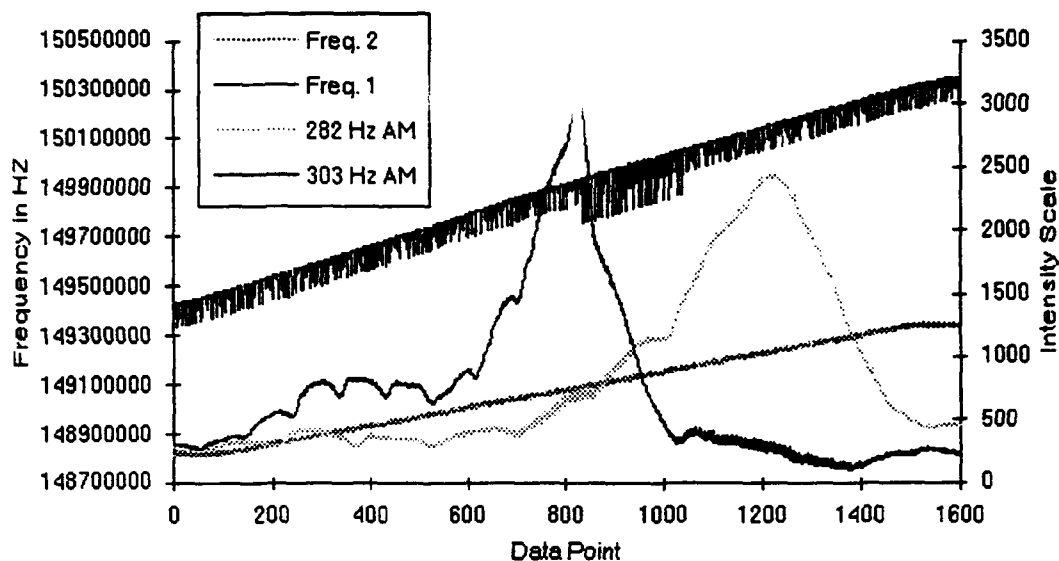


Figure 4.20. Wavelength scan on both laser diodes with a sinusoidal AM. LIA was set at $Q = 100$, the intensity scale is 1 mV/4095 for both signals.

The plots in Figure 4.20 were obtained using two sweep generators. The data tagged Freq. 1 and Freq. 2 corresponds to the output of the RF sweep generators. The Freq. 1 plot corresponds to the 303 Hz signal and the Freq. 2 plot to the 282 Hz signal. Both of the generators were set to 100 mW of output power. The HP8620C (Freq. 1 plot) is an older model which has less accuracy than the HP8350B, as can be seen on the plot. Also the sweep range and speed can not be obtained as easily and precisely as the newer model. The peak power output of each laser can be easily distinguished in the plots. The SDL (previously the fixed signal) is the 282 Hz signal while the 303 Hz signal, now the Sharp's laser diode, is the 303 Hz signal. Note that whenever one of the signals is at its peak the noise increases in the other signal.

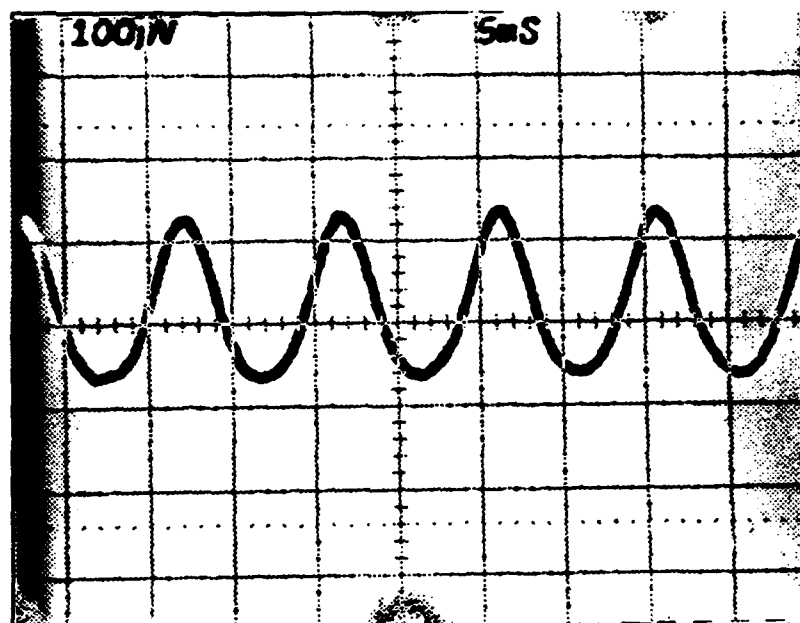


Figure 4.21. Detector output with single frequency present. The scales are 100 μ V/div and 5 mS/div.

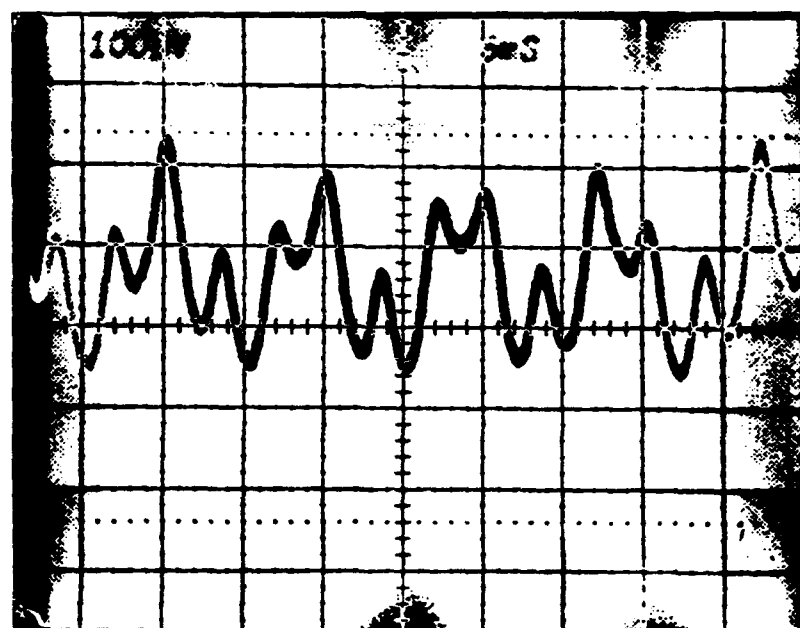


Figure 4.22. Detector output with multiple frequencies present. The scales are 100 μ V/div and 5 mS/div.

Figures 4.21 and 4.22 show the signals coming out of the detector. In Figure 4.21 only one signal is present, the 100 Hz AM. Note the irregular shape of the sinusoid, this is caused by the nonlinearities of Equation (3.43), see also Figure 3.12. As the frequency is increased the nonlinearity is reduced. Figure 4.21 shows the superposition of both signals, 100 Hz and 300 Hz, as seen by the detector.

5. RESULTS AND EVALUATION

This Chapter discusses the results obtained in the experiment as well as an evaluation of the system that is being analyzed. Figure 4.2 resembles the charging of a capacitor with a resistance in series, i.e., a low pass filter. The equation of a charging capacitor is of the form

$$V = a \left(1 - e^{\left(\frac{-t}{\tau} \right)} \right) \quad (5.1)$$

where a is the amplitude and τ is the rise time. From Figure 4.2 an estimate of a and τ can be made. Figure 5.1 shows the approximate mathematical function of Figure 4.2, using the estimates. This estimated function is given by:

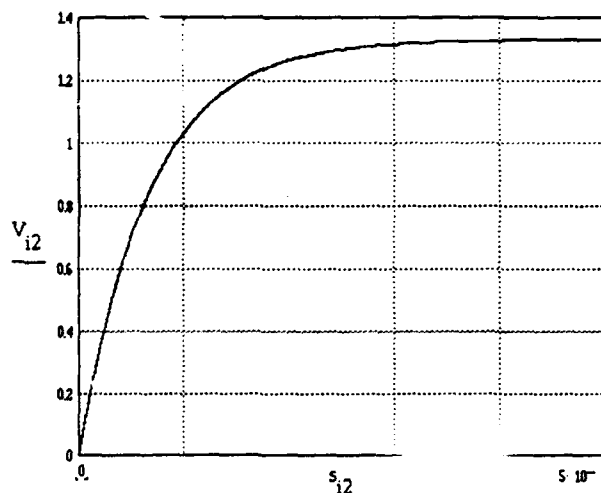


Figure 5.1. Theoretical response of the AUTF to a square wave modulation (Equation 5.2).

$$V = 1.33 \left(1 - e^{\left(\frac{-t}{6.7 \cdot 10^{-4}} \right)} \right) \quad (5.2)$$

where t is time and $\tau = 6.7 \cdot 10^{-4}$. Recalling that the frequency response of a low pass filter is given by:

$$\frac{1}{1 + S\tau} \quad (5.3)$$

where $S = j\omega$ then the modulating frequency response for this resonant structure is given by Figure 5.2. Using Figure 5.2, it can be seen that this AOTF can only be amplitude modulated up to a few hundred Hertz. From these data the modulation frequencies of the two signals were set one at 100 Hz and the other at 300 Hz.

The plot on Figure 4.5 has a FWHM about 7 times larger than what the manufacturer stated in the data sheet (3.1 Å). The broadening might have been caused in part by positioning the AOTF in the reverse direction changing the

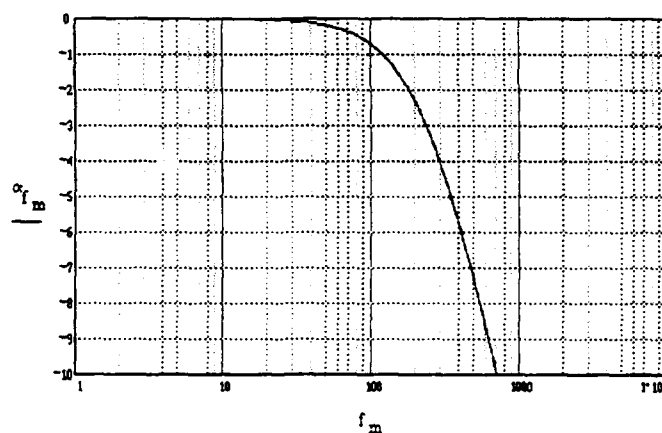


Figure 5.2. Modulating frequency response of the AOTF's resonant cavity.

incident angle for optimal performance (the faces of the crystal where the light enters and exits are not parallel to each other). But knowing the FWHM of one of the laser beams, SDL Figure 4.3, the FWHM of the AOTF's bandpass can be calculated. Using the Mathcad program on appendix B1, "Center Frequency Determination", and the plot for 282 Hz on Figure 4.20, the lower half maximum is obtained at ≈ 149.163 MHz (± 1 KHz, 828.293 ± 0.005 nm) and the upper half maximum is obtained at ≈ 149.298 MHz (± 1 KHz, 827.621 ± 0.005 nm). Which gives a FWHM of 0.672 nm. Recalling that in a convolution the width of the result is equal to the sum of the widths of the input functions, a FWHM for the AOTF's bandpass of 0.322 nm ($0.672 - 0.35$, from Figure 4.3) is obtained. Which is very close to the FWHM stated in the data sheet (3.1 nm). According to the Center Frequency Determination program a 1 KHz change in the RF frequency is equivalent to ≈ 0.005 nm change in the bandwidth, at these frequencies.

The lower half of the FWHM of the 282 Hz signal, on Figure 4.20, corresponds very close to the other frequency that the SDL will change to

Table 5.1. FWHM calculation of the AOTF

	<u>RF ± 1 KHz</u>	<u>Optical wavelength</u>
Peak	149.242 MHz	827.900 nm
Lower Half	149.163 MHz	828.293 nm
Upper Half	149.298 MHz	827.621 nm
Difference	- 00.135 MHz	0.672 nm
Laser's FWHM		0.35 nm
AOTF's FWHM		0.322 nm

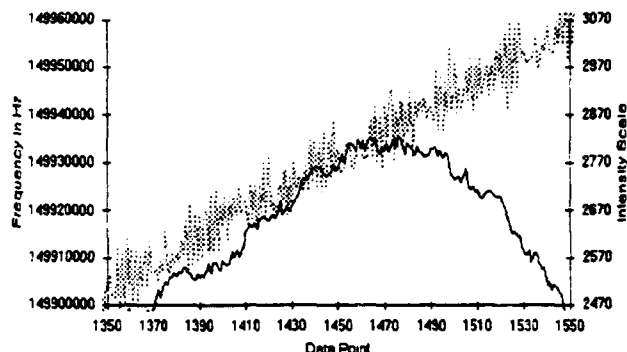


Figure 5.3. Zoom of the peak portion of the data on Figure 4.17.

sporadically. The wavelength change that the SDL incurs is about 0.4 nm (79 KHz) which was easily detected by the AOTF (using the CW RF generator). To determine the frequencies corresponding to the Sharp's LD peak output was more difficult due to the noise present in the sweeping generator, see Figure 5.3. In order to estimate the frequencies, the data were filtered using a Fast Fourier Transform (FFT) low pass filter program on Mathcad, see appendix B2. Once the data were filtered it was much easier to estimate the frequencies, Figure 5.4. As you can see the p-p amplitude of the noise from the RF signal, Figure 5.3, was

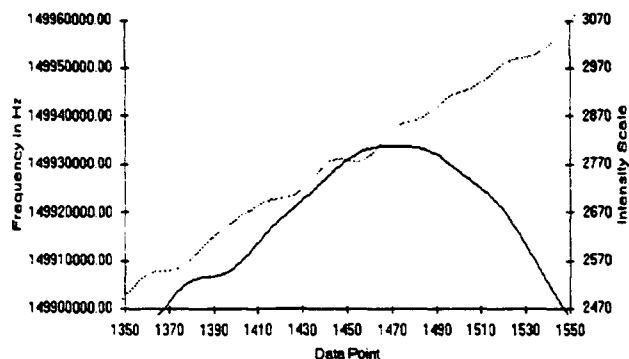


Figure 5.4. The data on Figure 5.3 after filtering.

approximately 13 KHz and after filtering the noise was almost gone. Using the data on Figures 4.17 and 4.18, after filtering, it was estimated that the RF frequencies where the maximum, for the Sharp's LD plot, occurs were approximately 149.937 and 149.660 MHz ($\pm 3 - 4$ KHz on both due to measurement errors), respectively. These frequencies correspond to (calculated with the "Center Frequency Determination" program) 824.457 and 825.825 nm ($\pm 0.015 - 0.02$ nm), respectively. The frequency counter was set to a resolution of 1 KHz (0.005 nm) and has an accuracy, at this resolution, of ± 1 KHz (± 0.005 nm).

The closest that the two signals were from each other was 418 KHz (approximately 2.08 nm). Due to the bandpass waveshape this separation is not enough to neglect the errors due to the sideband's crosstalk, see Section 3.3.1. The width of the first half of the 282 Hz data on Figure 4.20 is ≈ 424 KHz. This is the minimum distance (equal to the lower half of the AOTF's bandpass plus the

Table 5.2. Measurement Errors

	<u>RF frequency</u>	<u>Wavelength</u>
RF counter accuracy	± 1 KHz	± 0.005 nm
RF sweeper noise	$\pm 3-4$ KHz	$\pm 0.015-0.02$ nm
sidelobe crosstalk		$> \pm 0.05$ nm (minimum distance)

upper half of the SDL's optical signal) before both optical beams are within the main lobe, assuming that the large sidelobe is part of the main lobe. This will create an error in determining the peak wavelength in the lower wavelength diode (Sharp's diode) greater than ± 0.05 nm, at this minimum separation. This would not be the case for the upper wavelength diode (SDL's diode) because there is no large sidelobe in the lower wavelength side of the AOTF's bandpass. Only when one of the laser diodes is on or when measuring the SDL's diode alone can the wavelength be calculated with little or no concern on the sidelobe interference. When the Sharp's diode is at the lower wavelength, as in the case of Figure 4.20 which is at a 695 KHz separation from the SDL's peak wavelength, the crosstalk error will produce at most a ± 0.02 nm error in its peak wavelength determination, assuming the same efficiency as in Figure 4.2 Section 3.3.1.

The finite bandwidth of the LIA will create an additional crosstalk between the two AM channels. When the two AM signals are close to each other the LIA won't be able to completely separate the two channels. This crosstalk would create an error in the amplitude of the channel's signal. This can be noted on Figures 4.11, 4.12, and 4.17 - 4.19. But especially on Figures 4.12, 4.15, 4.16, and 4.18. These figures clearly illustrate the crosstalk between the channels. Because of the crosstalk, the oscillating noise, along with the signal, in the RF sweeper channel is coupled to the non-sweeper channel producing the observed noise. The amplitude of this crosstalk noise is dependent on how close the two signals are to each other and the relative amplitude between the signals. This is

also true for the AM harmonics created in each channel, see Figure 3.12. Another factor influencing the noise is the wave shape. As noted on Figures 4.11 and 4.12, a sinusoidal modulating wave will produce less crosstalk than a square modulating wave. Another type of noise that needs to be taken into account is thermal variations on the AOTF's crystal (TeO_2 for this case). Thermal variations will create slight variations in the index of refraction of the crystal, thus giving different bandpass peaks for the same frequency (but at different temperatures). For example, it was estimated^[11] that for a LiNbO_3 integrated AOTF^[11] a temperature controller with a 0.01°C stability is needed to obtain precisely repeatable drive frequencies. Otherwise a slight variation in the center frequency will be noted.

On Figure 4.6 it was impossible to measure β_1 (Equation (3.42)). You can also notice that the RF mixing by itself is non-linear and also produces two tone third order signals ($2f_1 - f_2$) thus increasing the noise at these harmonics, see Figures 4.8 and 4.9. At worst the SNR due to the two, RF and acoustic signals, two tone third order is 8.5 dB.

The maximum channel sweep speed will now be determine. If the filtered data is used, Figure 5.4, the smallest feature size is then 28 data points. In AM, the carrier frequency needs to be greater than the modulation frequency to be able to retrieve the modulated information. For this analysis two wavelengths will be chosen to describe the minimum features. On Figure 4.17 the scanning rate ($\Delta f/\Delta s$) was approximately 6 KHz/s ($\approx 600 \text{ KHz}/100 \text{ s}$). Each sample was taken

at approximately 0.045 s (100 s/2273 samples). This would make the scanning rate ($\Delta f/\Delta \text{sample}$) be 270 Hz/sample. A 28 sample step would cover a frequency change of approximately 7.56 KHz. In order to accommodate at least two AM carrier wavelengths in this span it should take $2T$, where T is the period of the carrier wavelength. Therefore the maximum scanning rate of the sweep generator is $7.56 \text{ KHz}/2T$. A FBG has a channel width of 4 nm, which is approximately 800 KHz width. With this the total time it will take to read a single channel can be calculated. For example, for a 100 Hz AM carrier ($T = 0.01 \text{ s}$) the maximum scanning rate is 378 KHz/s. The total time it would take to scan the FBG channel width would be 2.12 s. If the frequency is increased to 250 Hz the time is reduced to 0.85 s. But the frequency cannot be increased forever because of the resonance, see beginning of this chapter.

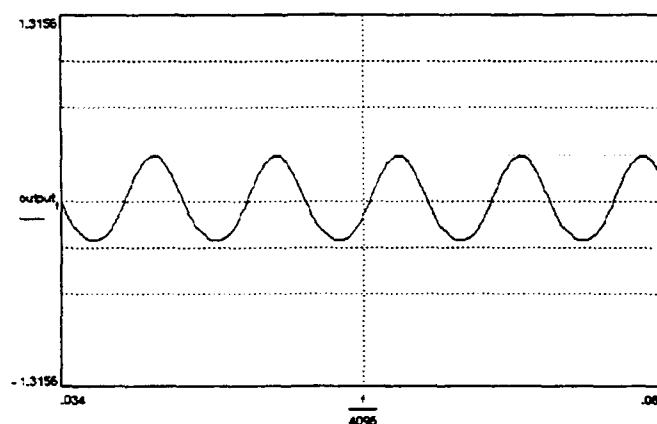


Figure 5.5. Mathematical model of the AOTF output at 105 Hz AM frequency.

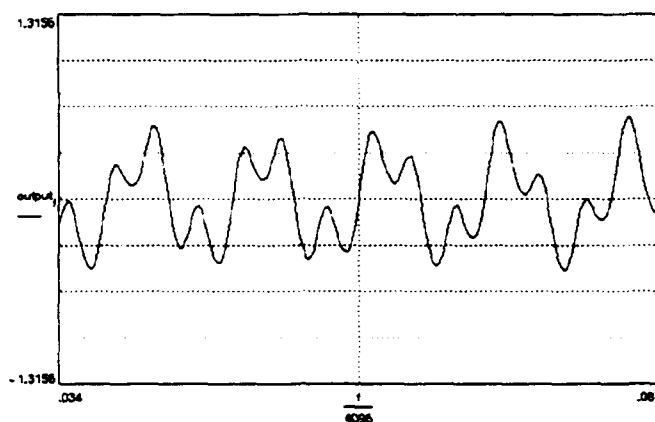


Figure 5.6. Mathematical model of the AOTF output with two signal input, 105 and 298 Hz AM frequency.

Using Equations (3.7), (3.38), and (5.2) a Mathcad program, appendix B3, was created to simulate the output of the AOTF. Figures 5.5 and 5.6 illustrates the results. The results were very similar to Figures 4.21 and 4.22. Thus showing that indeed the AOTF acts as a low pass filter that limits the maximum scanning speed.

Figure 5.7 illustrates the calculated bandpass of the LIA and Appendix A shows the manufacturer's data. This bandpass determines how well the LIA

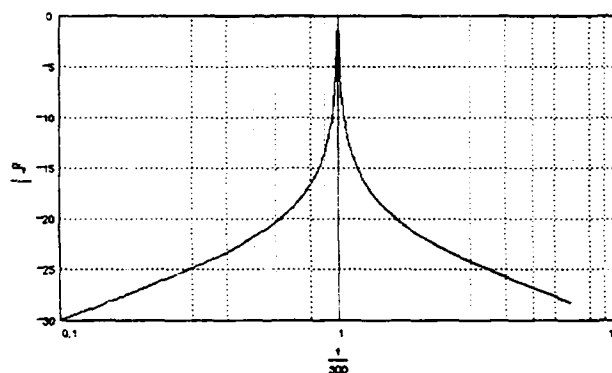


Figure 5.7. Calculated bandpass of the LIA, amplitude is in dB.

attenuates signals different than the center frequency. The crosstalk between AM frequencies, as discussed earlier, limits how close the two can be and their position in wavelength. In addition to the LIA, the crosstalk depends also on the relative intensities between them. For this system, with the intensities approximately equal and the high frequency set at 300 Hz, a $0.13 f_0$ (40 Hz, f_0 is the bandpass center frequency) sinusoidal modulation would be the minimum separation between channels. This separation will induce a 14.5 dB attenuation to the unwanted AM channel, see Figure 5.7.

The shape of the AOTF's bandpass deviated from the theory. This wave shape deviation will cause crosstalk errors greater than what was stated in Section 3.2. The magnitude of these errors depends on the relative amplitude between the optical signals. The minimum separation between the optical signals before there is crosstalk interference, due to the main lobe and the large lobes, with each other is illustrated in the shaded portion shown on Figure 5.8. On our

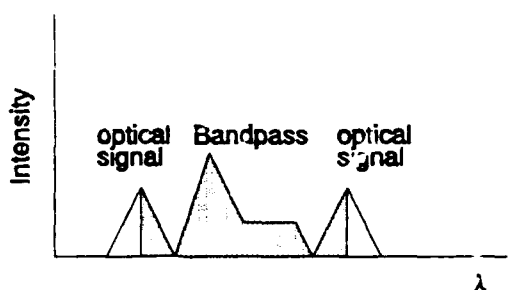


Figure 5.8. Minimum distance between optical signals.

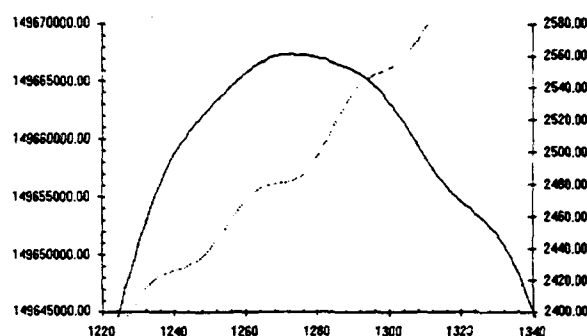


Figure 5.9. Zoom and filtering of the data on Figure 4.15.

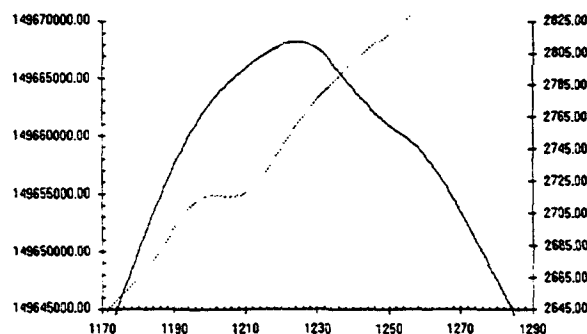


Figure 5.10. Zoom and filtering of the data on Figure 4.18.

experiment, this minimum distance was met only when the peak wavelength of both laser diodes were at their maximum separation (≈ 775 KHz, ≈ 3.875 nm). An illustration on the error in determining the wavelength peak of the optical signals is shown on Figures 5.9 and 5.10. Even when the minimum separation between the optical signals is met there is always error in determining the peak because of the sidelobe crosstalk.

6. CONCLUSION

Through this thesis, the effects of the harmonics on the output signal of the AOTF have been established. Also the ability of the AOTF to scan Multiple (two) AM modulated channels have been demonstrated and the limitation of the current design have been exposed. Its accuracy, at least theoretically, is similar to a quarter meter commercial spectrometer (IntraSpec III). In speed, for one and two channels, the AOTF and the IntraSpec II are comparable. Only the IntraSpec III is capable of more than two channels, with enough detail. The current AOTF design is capable of two with approximately 20 - 25% efficiency in each channel, after polarization. In compactness and ruggedness the AOTF is superior to the spectrum analyzer.

One of the limiting factors in using the AOTF to filtered multiple wavelengths is the power budget limitation. For this experiment the AOTF had 60% diffraction efficiency for polarized light, e- or o-polarized, at 500 mW, the maximum power input. In order to squeeze two channels into the AOTF the power output per RF generator had to be reduced to 200 mW. If $\approx 100\%$ of that energy went to the fundamental frequency it would have a diffraction efficiency for polarized light of $\approx 28\%$. With this efficiency the optical power needed, at the optical bandpass, would have to be large, the detector very sensitive or both. The super radiant diode didn't have the sufficient power nor did the detector have the sensitivity to

overcome all the losses of the system. To be able to accommodate a greater number of channels, a more efficient (%/mW) AOTF design is needed.

For this experiment the error in determining the peak wavelength came from the superposition of the AOTF's sidelobe, the sweeper noise, the temperature variations across the TeO_2 crystal (not measured because of equipment limitations) and the two-tone third-order harmonics. As stated in the previous paragraph (and in Table 5.2), the large sidelobe contributes to a great portion of the peak wavelength determination error. With an AOTF of the same design as used in this experiment (but with no large sidelobe, as the original AOTF) the crosstalk error due to the sidelobes would be at least ± 0.02 nm (assuming the same parameters as in Figure 3.12). In order to improve the precision, a more precise sweeper (or a fast stepper frequency synthesizer) with an accuracy of ± 1 KHz should be used, with a lower oscillating noise. The temperature variations along the AOTF can be controlled with a TE cooler added to the AOTF design. No two-tone third-order harmonics were detected.

A comparison will now be made between the AOTF and a commercial spectrometer, IntraSpec III quarter meter system. In a spectrometer the light coming from the signal falls into a grating where it is diffracted. The diffracted light will fall in a detector, or array of detectors, which is placed at a particular location. The wavelength scan is made by physically rotating the grating. In the IntraSpec III system a 1024 cooled diode array detects the light diffracted by the grating and depending on which diode you are looking will be the wavelength.

The array has a resolution of 0.062 nm, each diode is separated in wavelength by this amount, for a total window of 63.6 nm. Each element (pixel) of the array can be read at a maximum rate of 110 KHz. In order to read the signals the array needs a minimum exposure time of 1 s. With this system 10 FBG channels could be scanned simultaneously, assuming that the channels have a width of 5 nm. This system has been used to scan a FBG using a xenon lamp acting as a broad band optical source. In order to compare this system with the AOTF, it will be assumed that a sensitive detector is used (e.g., PMT) and that incremental steps of 12 KHz are taken. The total number of steps would be 67 ($800/12$, see Chapter 5). The slowest frequency to be used would be 250 Hz for the dual channel scanning. At each step the waiting period will be $2 T$ (T is the period, 0.008 s). The speed at which the whole channel(s) can be read is 0.536 s. Since it is reading two channels simultaneously it could read approximately 4 channels per second. Speed wise this AOTF would be slower than the mentioned spectrometer for a given window. In order to change windows, the operator would have to physically rotate the spectrometer's grating.

In summary the AOTF system offers little or no advantage over the commercially available IntraSpec III system. Further design improvements are needed to increase the AOTF speed. The speed would increase if the resonance effect is eliminated or its cutoff frequency, see Chapter 5, is increased. The temperature variations could be controlled by incorporating a TE cooler to the design.

7. FUTURE WORK

To improve the performance of the AOTF, a new design has to be made in which there is no resonance, or that the cutoff frequency, due to the resonance, is higher (preferably in the 10s of KHz). This new design should also be more efficient power wise (% diffraction per mW of RF power), so that multiple channels can be used. Using amplitude modulation will make it difficult to implement multiple channel. This is due to the fact that the signal and harmonics of one channel should be kept at a minimum distance ($\approx 0.13 f_o$, where f_o is the AM frequency of the other channel) from the other AM channels to reduce crosstalk.

A possible alternative to use AM modulation would be to investigate the possibility of using optical heterodyning, as pointed by Equation (3.12), to separate the sensor channels. In this approach some problems might arise, like for example the coherence length, and it should be investigated further. Another alternative would be using frequency modulation instead of amplitude modulation. This should minimize some of the problems as well as provide some of its own. A totally different alternative would be to develop a fast scanning laser that would scan all the sensors (5-10) in a short amount of time. But this would require a tuning range of at least 30 nm.

REFERENCES

- [1] Anthony Dandridge, "Fiber-Optic sensors make waves in acoustics, control, and navigation", IEEE Circuits & Devices, 6(6), 12 - 19, Nov. 1990.
- [2] R M Measures et al, "Wavelength demodulated Bragg grating fiber optic sensing system for addressing smart structure critical issues", Journal of Smart Materials and Structures, 1, 36-44. 1992.
- [3] J. R. Dunphy, G. Meltz, F. P. Lamm and W. W. Morey, "Multi-function, distributed optical fiber sensor for composite cure and response monitoring", Fiber Optic Smart Structures and Skins III, SPIE 1370, 116 - 118, 1990
- [4] United Technologies Photonics Application Notes for Fiber Optic Bragg Gratings. Jan 1991
- [5] W. W. Morey, G. Meltz, and W. H. Glenn, "Fiber optic Bragg grating sensors", Fiber Optic and Laser Sensors VII, SPIE Press, 1169, 98-107. 1989
- [6] Norman J. Berg and John N. Lee, "Acousto-Optic Signal Processing: theory and implementation", MARCEL DEKKER, INC., New York, NY, 1983.
- [7] Eugene Hecht, "Optics" second edition, Addison-Wesley Publishing Company, Inc., Reading, Mass, 1989.
- [8] Francis Boero, "SPECTRUM ANALYZERS ADVANCE TO ULTRAHIGH-RESOLUTION PERFORMANCE", Laser Focus/Electro-Optics, pp 120, March 1988.
- [9] Yaolu Wang, "Acousto-optic tunable filters spectrally modulate light", Laser Focus World, 28(5), 173 - 180. May 1992.
- [10] I. C. Chang, "Tunable Acousto-optic Filters: An Overview", Optical Engineering, 16(5), Sep./Oct. 1977.

- [11] K. W. Cheung, D. A. Smith, J. E. Baran, and B. L. Heffner, "Multiple channel operation of an integrated acousto-optic tunable filter", *Electronics Letters*, 25, 375 - 376, 1989
- [12] D. K. W. Lam and B. K. Garside, "Characterization of single mode optical fiber filters", *Applied Optics*, 20(3), 440 - 445, Feb. 1981
- [13] Zhong-Yi Yin, Paul E. Jessop, and Brian K. Garside. "Photoinduced grating filters in GeO_2 thin-film waveguides", *Applied Optics*, 22(24), 4088 - 4092, Dec. 1983
- [14] Amnon Yariv, "Optical Electronics", CBS College Publishing, New York, NY. 1985
- [15] Adrian Korpel, "Acousto-Optics", MARCEL DEKKER, INC., New York, NY 1988
- [16] I. C. Chang, "Noncollinear acousto-optic filter with large angular aperture", *Applied Physics Letters*, 25(7), 370-372 Oct. 1974.
- [17] I. C. Chang, "Acousto-optic tunable filters", *Optical Engineering*, SPIE press, 20(6), 824-829 Nov./Dec. 1981
- [18] I. C. Chang, "Analysis of the noncollinear Acousto-Optic filter", *Electronics Letters*, 11(25/26), 617 - 618 Dec., 1975
- [19] I. C. Chang, "Acoustooptic Devices and Applications", *IEEE Transactions on Sonics and Ultrasonics*, su-23(1), 2 - 22, Jan 1976
- [20] S. E. Harris and R. W. Wallace, "Acousto-optic tunable filter", *J. Opt. Soc. Am.* 59(6), 744 - 747, June 1969.
- [21] I. C. Chang, "Multifrequency acousto-optic interaction in Bragg Cells ", *Acousto-Optic, Electro-Optic, and Magneto-Optic Devices and Applications*, SPIE press, 97 - 102, 753, 1987.
- [22] Pankaj K. Das and Casimer M. DeCusatis, "Acousto-Optic Signal Processing: Fundamentals & Applications", Artech House, Inc., Norwood, MA, 1991
- [23] Eddie H. Young, jr. and Shi-Kay Yao, "Design Considerations for Acousto-Optic Devices", *Proceedings of the IEEE*, 69(1), 54 - 64 Jan. 1981.

- [24] I. C. Chang, P. Katzka, J. Jacob, S. Estrin, "Programmable Acousto-Optic Filter", 1979 IEEE Ultrasonics Symposium Proceedings, 221(1980), 40 - 45, Sep. 1979.

APPENDIX A: LIA BandPass Characteristics.

The Lock-In-Amplifier model 124A from Princeton Applied Research Co. accurately measures the rms amplitude and phase of weak signals buried in noise. Signals in the range of picovolts up to 500 millivolts at frequencies from 0.2 Hz to 210 kHz can be measured quickly and precisely. These measurements are with reference to a synchronizing signal supplied to, or supplied by, the Model 124A. The following figures illustrate the phase and frequency characteristics of the Model 124A in bandpass mode.

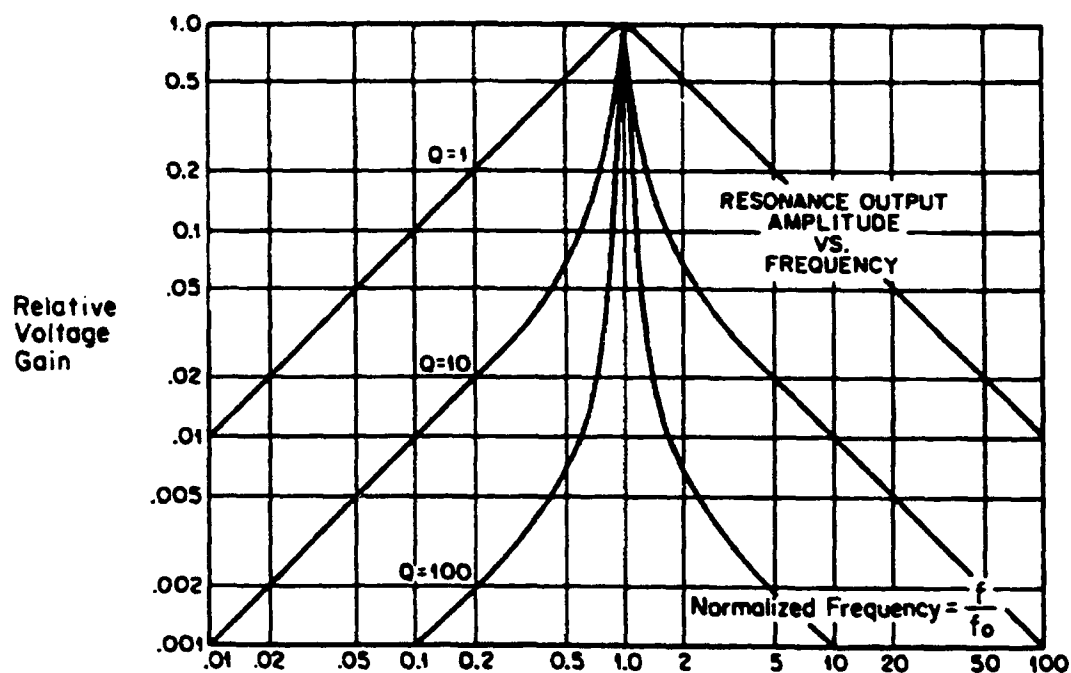


Figure A.1. Frequency bandpass characteristics of the LIA Model 124A, as stated by the manufacturer.

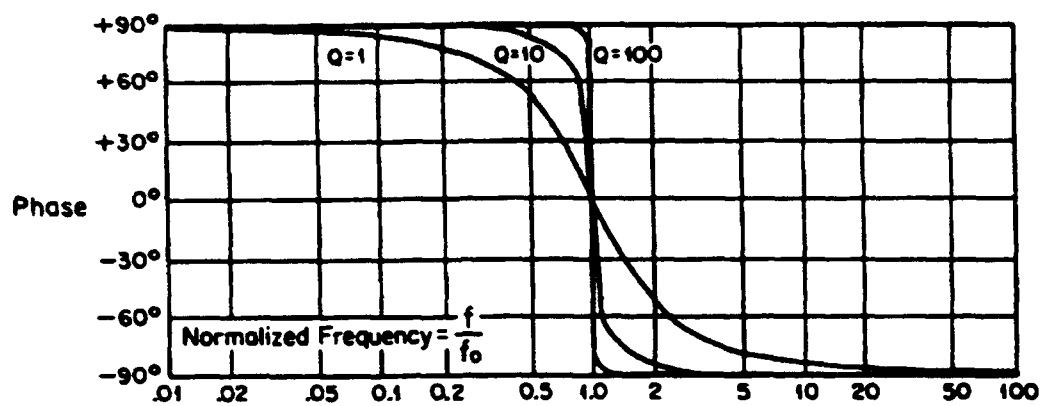


Figure A.2. Phase bandpass characteristics of the LIA Model 124A, as stated by the manufacturer.

APPENDIX B1: Center Frequency Determination Program

$$c := 2.998 \cdot 10^8 \quad \text{Velocity of light in a vacuum}$$

$$j := 1.602 \cdot 10^{-19}$$

$$\lambda := 827.9 \cdot 10^{-9} \quad \text{Wavelength in vacuum}$$

$$L := 19 \cdot 10^{-3} \quad \text{Interaction length between the acoustic and the optical beam}$$

$$V_a := 914.056 \quad \text{Acoustic velocity}$$

$$f_a := 149.242 \cdot 10^6 \quad \text{Acoustic frequency}$$

$$\theta_i := 31.015 \cdot \frac{\pi}{180} \quad \text{Incident optical angle, with the optical axis}$$

$$\theta_a := \text{atan}(2 \cdot \cot(\theta_i)) + \theta_i \quad \text{Acoustic angle, with the optical axis}$$

Calculation of the refraction indices for TeO//2

For the wavelength region 400 - 1000 nm at 20 deg. C

$$E := \frac{4.136 \cdot 10^{-15} \cdot j \cdot 2.998 \cdot 10^8}{1.602 \cdot 10^{-19} \cdot \lambda}$$

$$n_o := \sqrt{\frac{220.6}{9.24^2 - E^2} + \frac{25.55}{4.70^2 - E^2} + 1}$$

$$n_e := \sqrt{\frac{241.0}{9.24^2 - E^2} + \frac{34.20}{4.71^2 - E^2} + 1}$$

$$n_o = 2.2228126$$

$$n_e = 2.3693857$$

$$\text{Dnz} := n_e - n_o$$

$$\text{Dnz} = 0.1465730883$$

$$\theta_a \cdot \frac{180}{\pi} = 104.2837755506$$

$$\lambda_4 := \left[\frac{V_a \cdot \text{Dnz}}{(f_a)} \right] \cdot \sqrt{(\sin(\theta_i))^4 + \sin(\theta_i \cdot 2)^2}$$

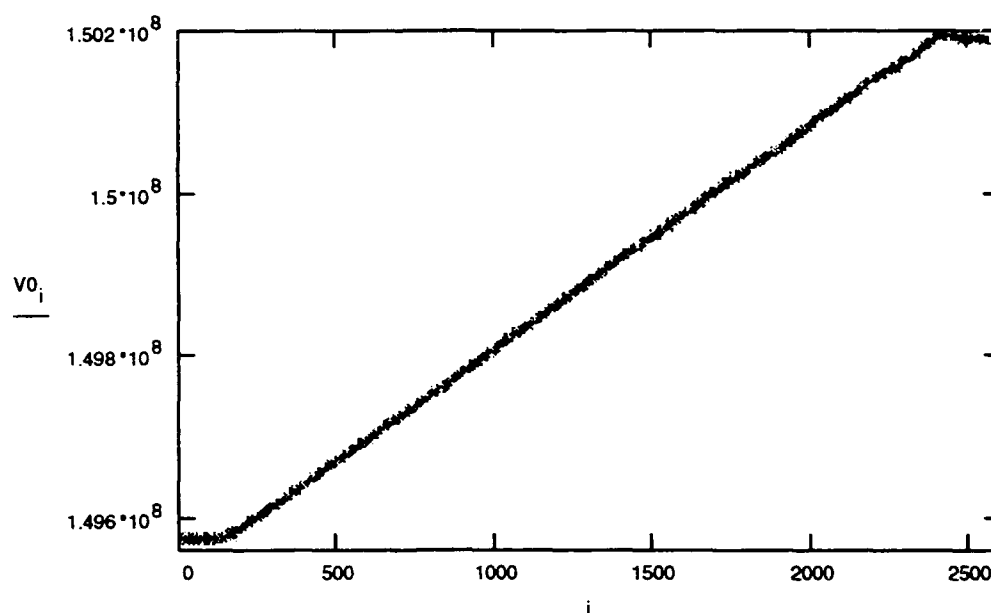
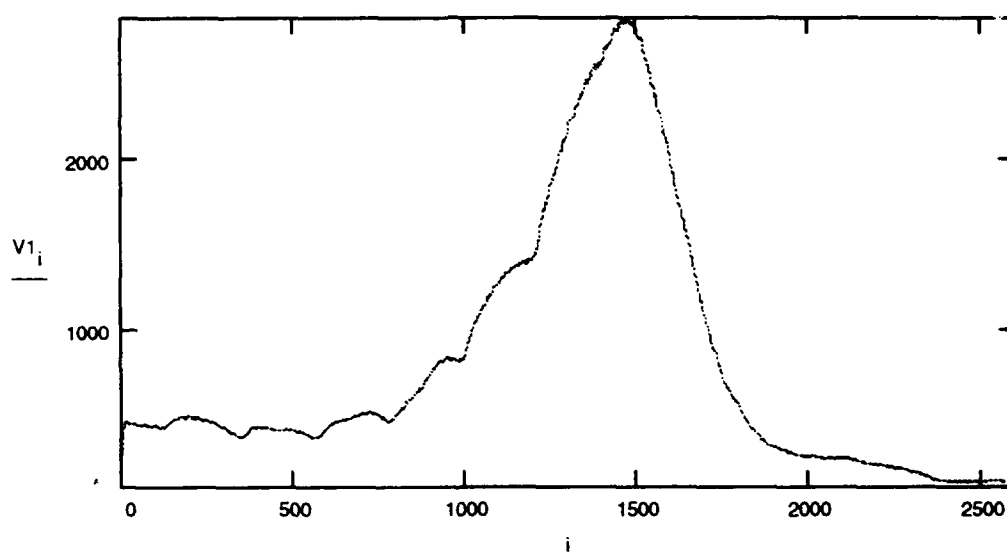
$$\lambda_4 \cdot 10^9 = 827.8998148$$

APPENDIX B2: Data Filtering Program

$M := \text{READPRN}(\text{cmix23})$ Input from file cmix23.fit

$V0 := M^{<0>}$ $V1 := M^{<1>}$ $V0$ is the RF frequency and $V1$ the amplitude of the signal

$z := \text{last}(V1)$ $i := 0..z$

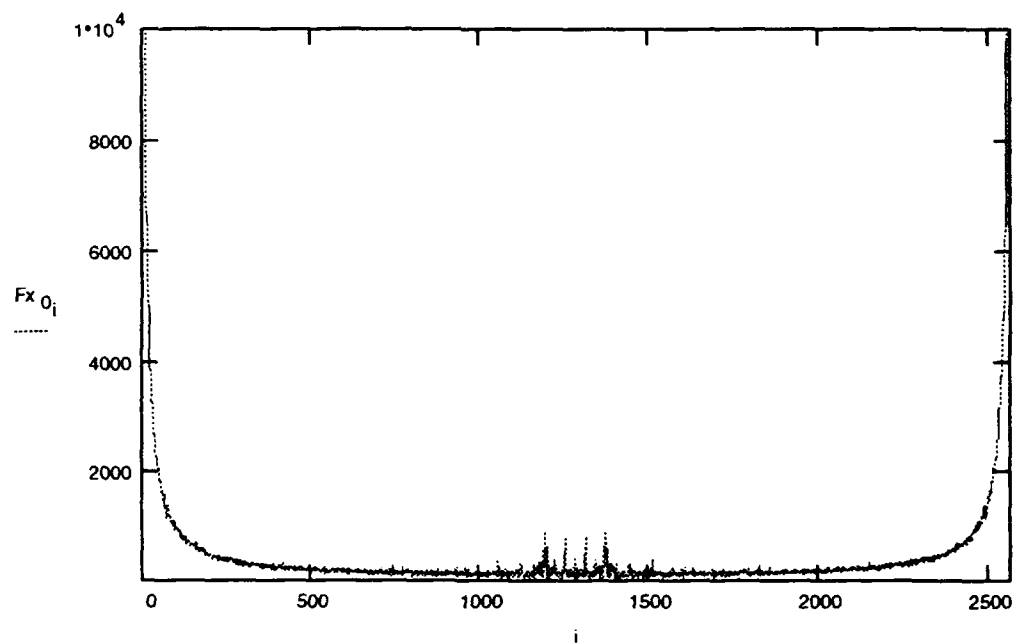
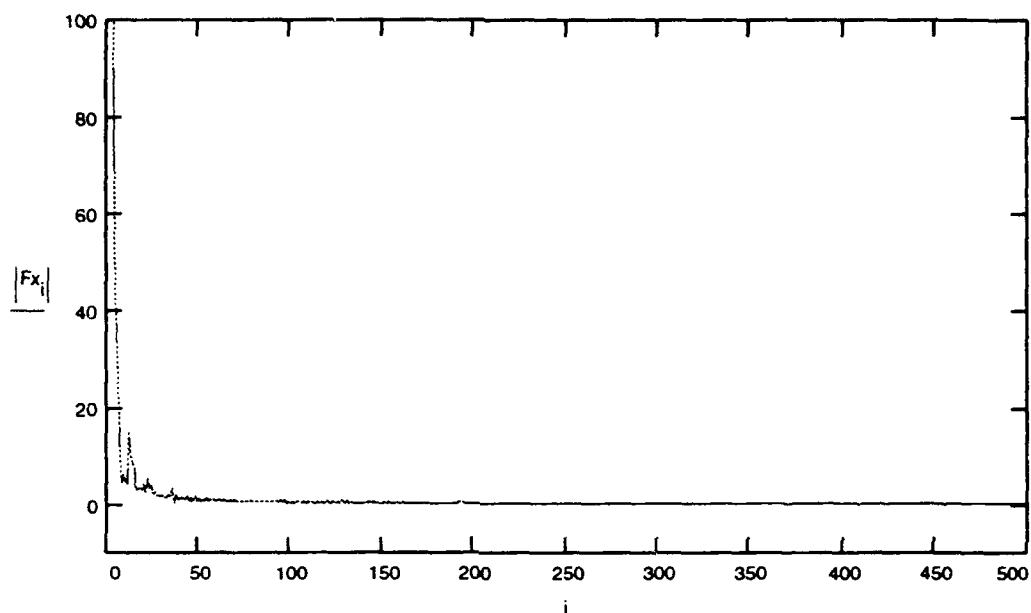


$Fx0 := \text{CFFT}(V0)$

$Fx0$ and Fx are the FFT of $V0$ and $V1$ respectively

$Fx := \text{CFFT}(V1)$

$Fx_{0_i} := \text{if}(|Fx0_i| \leq 10000, |Fx0_i|, 10000)$



cutof1 := 90 cutof := 110 The smallest period that is passed would be
 $2568/\text{cutof}^*$

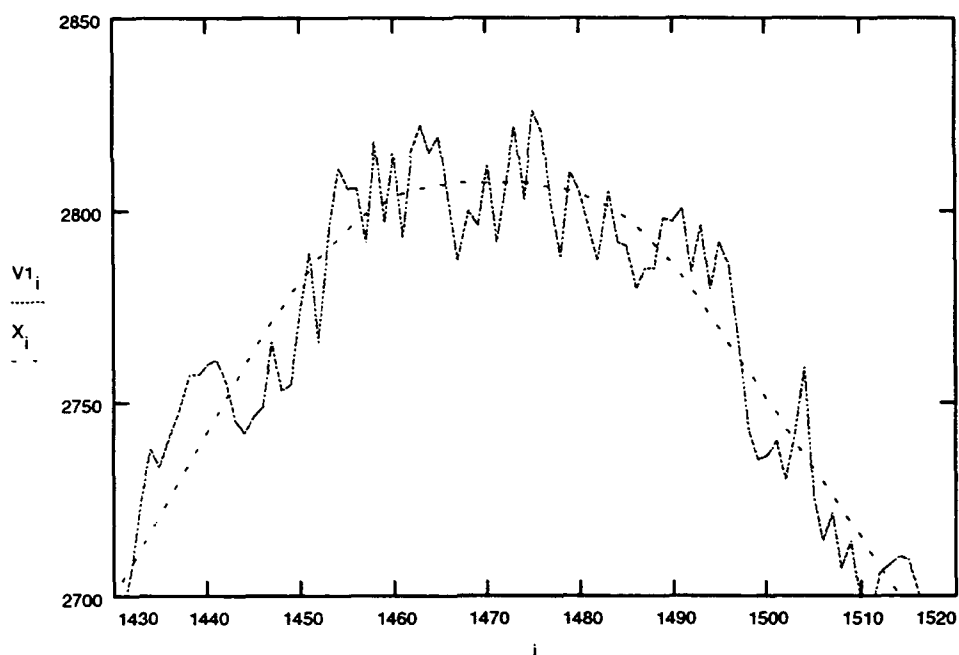
$W(i) := \text{if}(i \leq \text{cutof1}, 1, \text{if}(i \geq z - \text{cutof1}, 1, 0))$ $W(i)$ and $W1(i)$ are the bandpass functions

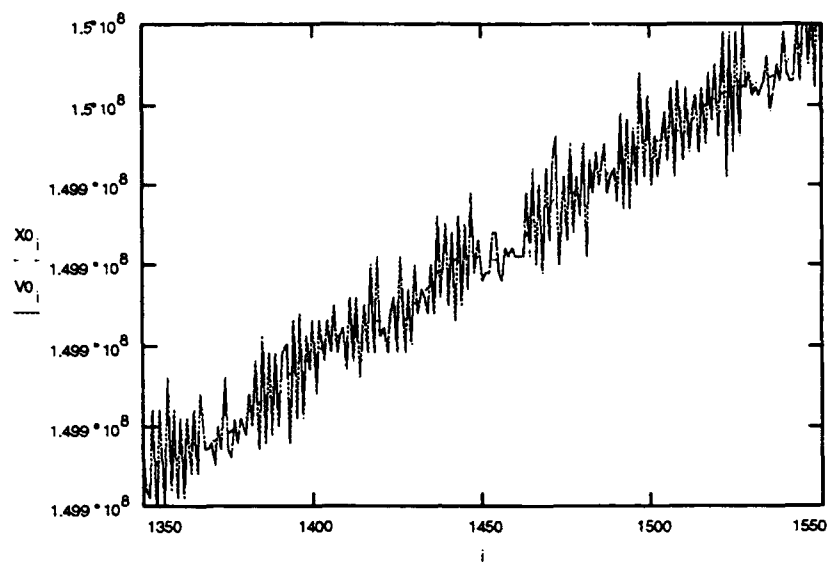
$W2(i) := \text{if}(i \leq \text{cutof}, 1, \text{if}(i \geq z - \text{cutof}, 1, 0))$

$Fx_i := W(i) \cdot Fx_i$ Fx and $Fx0$ are being filtered

$Fx0_i := W2(i) \cdot Fx0_i$

$X := \text{ICFFT}(Fx)$ X and $X0$ are the inverse FFT of Fx and $Fx0$. These two are the filtered
 $X0 := \text{ICFFT}(Fx0)$ functions of $V1$ and $V0$, respectively.





Procedure to store the filtered functions. The insignificant complex error is truncated.

```
X0 := Re( X0)      X := Re( X)
```

```
outmatrix := augment( X0, X)
```

```
PRNPRECISION := 11
```

```
PRNCOLWIDTH := 11
```

```
WRITEPRN( filtered ) := outmatrix a      output to file th23.ftt
```

APPENDIX B3: AOTF Simulation Program

$M_2 := 4.6559739 \cdot 10^{-14}$ Acousto-Optic figure of merit relating acoustic power with diffraction efficiency

$L := 19 \cdot 10^{-3}$ Interaction length between light and sound.

$H := 4 \cdot 10^{-3}$ Transducer (acoustic beam) height

$P := 200 \cdot 10^{-3}$ RF electrical (acoustic) power

$\lambda_o := 833 \cdot 10^{-9}$ Wavelength 1

$\lambda_{2o} := 838 \cdot 10^{-9}$ Wavelength 2

$i2 := 0 \dots 6000$

$i1 := 0 \dots 4095$

each increment in i is $1/(4096)$ s increments
With this each division in frequency is 1 hz

$$H1_{i1} := \left[1 \cdot \sin \left[\frac{\pi}{\lambda_o} \cdot \sqrt{M_2 \cdot L \cdot P \cdot \frac{\left(1 + .8 \cdot \sin \left(2 \cdot \pi \cdot 298 \cdot \frac{i1}{4095} \right) \right)^2}{2 \cdot H}} \right] \right]^2$$

Peak fractional transmission for wavelength 1

$$H2_{i1} := \left[1 \cdot \sin \left[\frac{\pi}{\lambda_{2o}} \cdot \sqrt{M_2 \cdot L \cdot P \cdot \frac{\left(1 + .80 \cdot \sin \left(2 \cdot \pi \cdot 105 \cdot \frac{i1}{4095} + \pi \cdot \frac{20}{180} \right) \right)^2}{2 \cdot H}} \right] \right]^2$$

Peak fractional transmission for wavelength 2

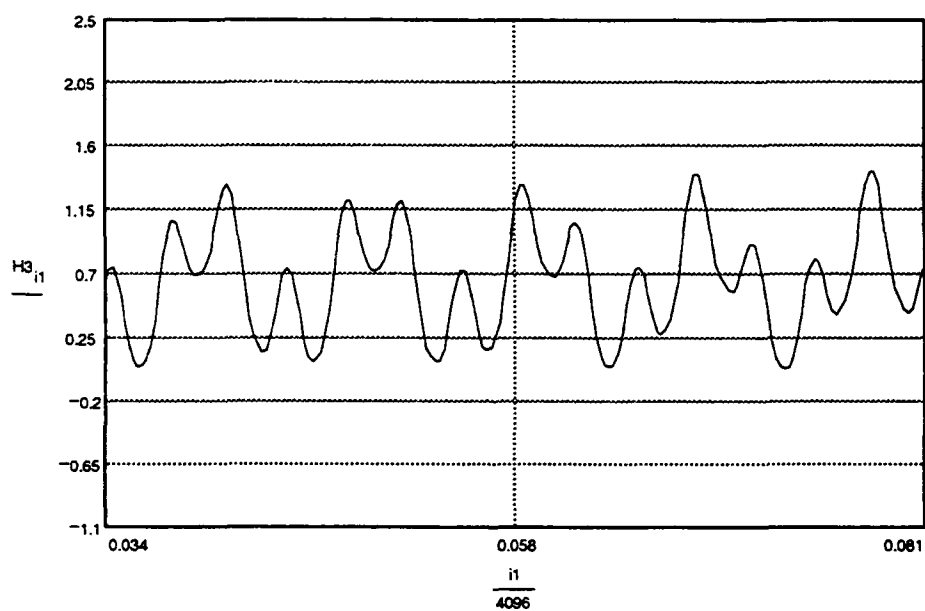
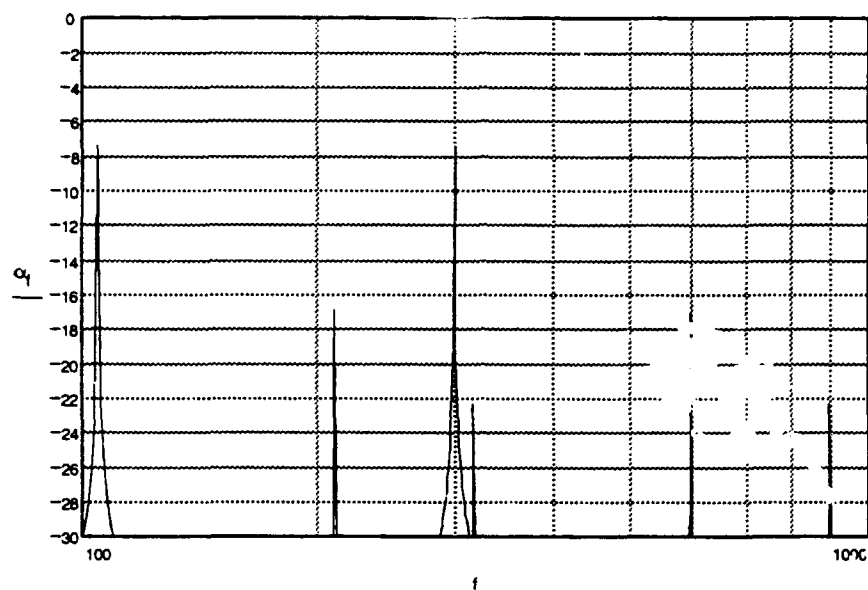
$H3_{i1} := H1_{i1} + H2_{i1}$ Superposition of both signals excluding harmonics.

$t := \text{FFT}(H3)$ Change to the frequency domain

$N := \text{last}(t)$

$f := 1 \dots N$

$\alpha_f := 10 \cdot \log(|t_f|)$ Amplitude of signals in dB

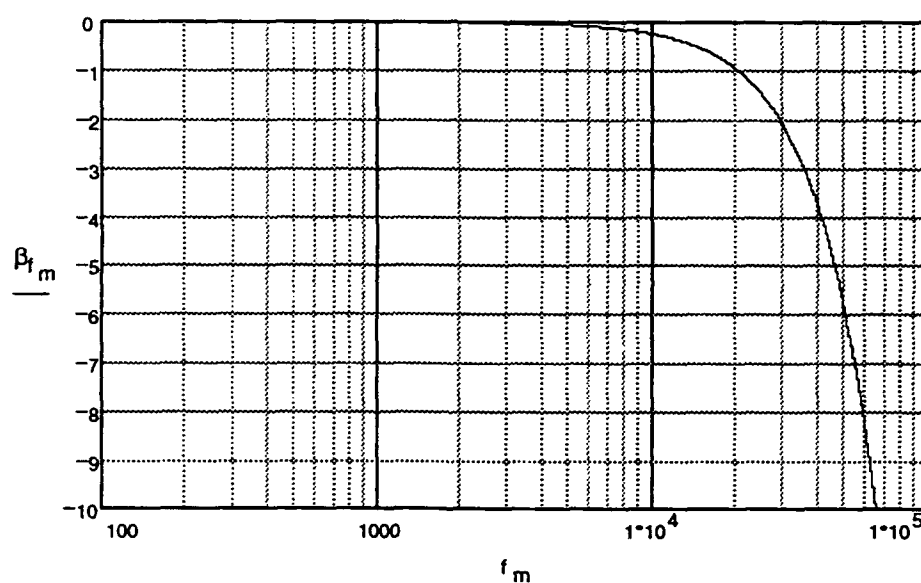


$$f_m := 1..70000$$

$$\tau := 21 \cdot 10^{-6} \quad \text{Transit time (optical aperture in unit time)}$$

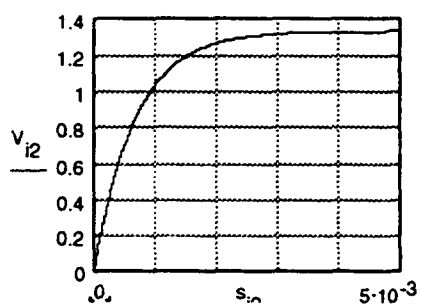
$$MTF_{f_m} := \exp \left[\frac{-\pi^2 \cdot (f_m)^2 \cdot \tau^2}{8} \right] \quad \text{Frequency response of an amplitude modulated Bragg cell}$$

$$\beta_{f_m} := 10 \cdot \log(MTF_{f_m}) \quad \text{Frequency response in dB}$$



$$s_{i2} := i2 \cdot 10^{-6} \quad \text{Time in microsecond increments}$$

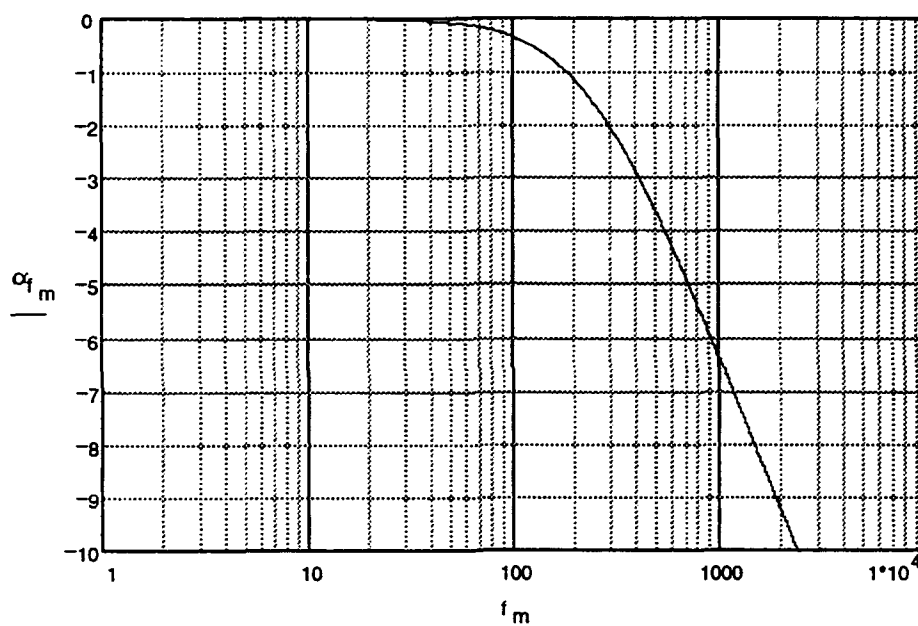
$$V_{i2} := 1.33 \cdot \left[1 - \exp \left[\frac{(-1 \cdot s_{i2})}{.67 \cdot 10^{-3}} \right] \right] \quad \text{Unit step response of the AOTF resonant cavity in time domain}$$



$$H_{f_m} := \frac{1}{1 + 2i \cdot \pi \cdot f_m \cdot (0.67 \cdot 10^{-3})}$$

AOTF's resonant cavity transfer function (in time domain)

$$\alpha_{f_m} := 10 \cdot \log(|H_{f_m}|)$$



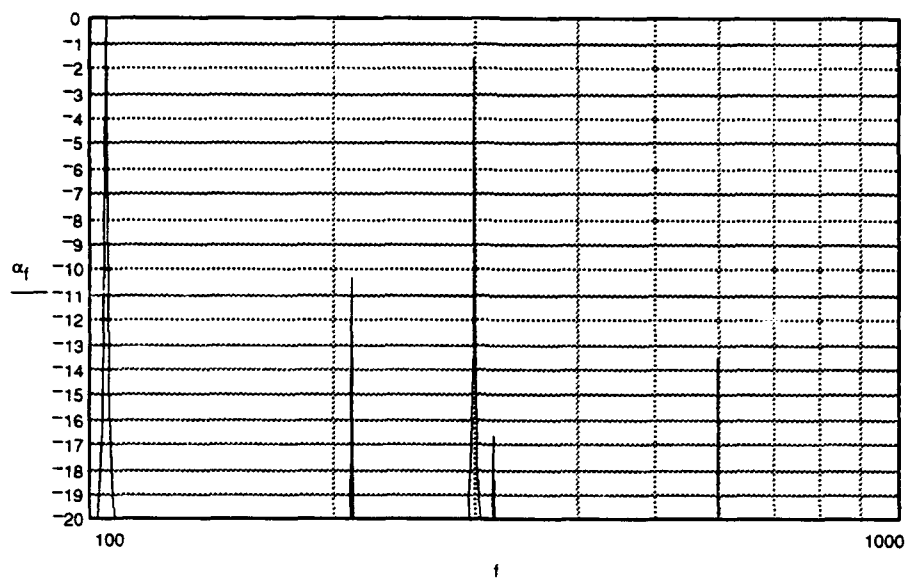
$$\text{pass}_f := t_f \cdot H_f \cdot \text{MTF}_f$$

$$\text{pass2}_f := |\text{pass}_f|$$

$$\text{maximo} := \max(\text{pass2})$$

$$\text{maximo} = 0.1653601$$

$$\alpha_f := 10 \cdot \log\left(\left|\frac{\text{pass}_f}{\text{maximo}}\right|\right)$$



output := IFFT (pass) Return to the time domain

